HHS Public Access

Author manuscript

Cancer Discov. Author manuscript; available in PMC 2021 May 01.

Published in final edited form as:

Cancer Discov. 2020 November ; 10(11): 1654–1671. doi:10.1158/2159-8290.CD-20-0442.

An *in vivo* KRAS allelic series reveals distinct phenotypes of common oncogenic variants

Maria Paz Zafra[1,*], **Marie J Parsons**[1], **Jangkyung Kim**[2], **Direna Alonso-Curbelo**[3], **Sukanya Goswami**[1], **Emma M Schatoff**[1,4], **Teng Han**[1,2], **Alyna Katti**[1,2], **Maria Teresa Calvo Fernandez**[1], **John E Wilkinson**[5], **Elena Piskounova**[1,6,7], **Lukas E Dow**[1,7,8,*]

[1]Sandra and Edward Meyer Cancer Center, Weill Cornell Medicine, New York, NY

[2]Weill Cornell Graduate School of Medical Sciences, Weill Cornell Medicine, New York, NY

[3]Cancer Biology and Genetics, Memorial Sloan Kettering Cancer Center, New York, NY

[4]Weill Cornell / Rockefeller / Sloan-Kettering Tri-Institutional MD-PhD program, New York, NY

[5]Department of Pathology, University of Michigan, Ann Arbor MI/Department of Comparative Medicine, University of Washington, Seattle WA.

[6]Department of Dermatology, Weill Cornell Medicine, New York, NY

[7]Department of Biochemistry, Weill Cornell Medicine, New York, NY

[8]Department of Medicine, Weill Cornell Medicine, New York, NY

Abstract

KRAS is the most frequently mutated oncogene in cancer, yet there is little understanding of how specific KRAS amino acid changes impact tumor initiation, progression, or therapy response. Using high-fidelity CRISPR-based engineering, we created an allelic series of new *LSL-Kras* mutant mice, reflecting codon 12 and 13 mutations that are highly prevalent in lung ($KRAS^{G12C}$), pancreas ($KRAS^{G12R}$) and colon ($KRAS^{G13D}$) cancers. Induction of each allele in either the murine colon or pancreas revealed striking quantitative and qualitative differences between KRAS mutants in driving the early stages of transformation. Further, using pancreatic organoid models we show that $KRAS^{G13D}$ mutants are sensitive to EGFR inhibition, while $KRAS^{G12C}$ mutant organoids are selectively responsive to covalent G12C inhibitors only when EGFR is suppressed. Together, these new mouse strains provide an ideal platform for investigating KRAS biology *in vivo* and for developing pre-clinical precision oncology models of KRAS-mutant pancreas, colon, and lung cancers.

* Correspondence: Lukas E. Dow, Belfer Research Building, 413 East 69th Street, BB1318, New York, NY, 10021, lud2005@med.cornell.edu, Ph: +1 646 962 6313, Maria Paz Zafra, Belfer Research Building, 413 East 69th Street, BB13-C01, New York, NY, 10021, mpz2001@med.cornell.edu, Ph: +1 646 962 6315 .

Author Contributions

MPZ designed and performed experiments, analyzed data and wrote the paper. MJP, JK, DAC, SG, EMS, TH, AK, MTCP, JW and EP performed experiments and/or analyzed data. LED designed, performed and supervised experiments, analyzed data, and wrote the paper.

Conflict of Interest Statement

LED is a scientific advisory board member for Mirimus Inc.

Keywords

Kras; LSL-Kras; CRISPR; PDAC; ADM; PanIN

INTRODUCTION

KRAS is the most frequently mutated oncogene in human cancers and considered a key early driver of many tumors. Specific cancer types show a clear bias in the types and frequency of *KRAS* alterations (1,2), and while carcinogen-specific mutational signatures define a subset of tissue-selective *KRAS* changes, they do not account for the majority of tissue-selective *KRAS* alterations (3,4). Biochemically, oncogenic *KRAS* mutations increase the abundance of GTP-bound 'active' KRAS protein, but different amino acid changes can significantly alter the kinetics of GDP/GTP exchange and GTP hydrolysis (5). Such changes may have implications for signaling dynamics in different cell or tissue contexts. Finally, mounting clinical and pre-clinical evidence suggests that tumors carrying distinct KRAS variants are differentially sensitive to targeted therapies (6–8). Thus, despite genetic and epidemiologic evidence that differences between *KRAS* mutations are functionally important, we still do not have a clear understanding of how distinct *KRAS* alterations dictate tumor initiation, disease progression, or response to therapy.

Conditional animal models, such as *Kras* $^{Lox\text{-}Stop\text{-}Lox\,(LSL)\text{-}G12D}$ and *Kras* $^{LSL\text{-}G12Vgeo}$ mice developed almost 20 years ago (9,10), have been critical tools for dissecting the role of *KRAS* mutations in tumor development. However, these models alone do not recapitulate the spectrum of *KRAS* alterations in human cancer. Here we describe an efficient pipeline for engineering an allelic series of conditional alleles that significantly expands the repertoire of pre-clinical KRAS-driven cancer models. Using high-fidelity CRISPR targeting in embryonic stem cells (ESC)-based mouse models (GEMM-ESCs) (11–14), we engineered six new *Kras* $^{LSL\text{-}mutant}$ alleles (G12V, G12C, G13D, G12R, G12A, and G12S) that represent the most frequent mutations at the G12/G13 hotspot, after G12D. Guided by clinical data, we generated conditional mice representing three tissue-selective alterations observed in colorectal ($KRAS^{G13D}$), pancreatic ($KRAS^{G12R}$), and lung cancer ($KRAS^{G12C}$) and show that, even subtle mutational changes in KRAS impact pre-malignant changes in the colon and pancreas.

In line with these diverse biological outputs *in vivo*, pancreatic organoids derived from these models uncovered KRAS variant-specific vulnerabilities. Specifically, we show that $KRAS^{G13D}$ mutant cells are sensitive to inhibition of the epidermal growth factor receptor (EGFR), and that combined treatment with RTK and covalent KRAS G12C inhibitors is required for potent growth suppression in $KRAS^{G12C}$ / p53 mutant organoids. Thus, these new animal models serve as a powerful pre-clinical resource to interrogate *KRAS* biology *in vivo* and develop rational strategies to effectively target specific KRAS mutant cancers.

RESULTS

A CRISPR-based pipeline for engineering *Kras* allelic variants in an established conditional allele

To engineer new $Kras^{LSL\text{-}mutant}$ alleles, we used CRISPR-mediated homology directed repair (HDR) to introduce specific codon 12/13 mutations into the well-characterized $Kras^{LSL\text{-}G12D}$ allele. For this, we took advantage of previously derived genetically engineered embryonic stem cells (GEMM-ESCs) (14) carrying the endogenous $Kras^{LSL\text{-}G12D}$ allele, with a pancreas specific Cre recombinase (*Ptf1a-Cre,* also known as *p48-Cre*) and a far-red fluorescent Cre-reporter (*CAGs-LSL-rtTA3-IRES-mKate2*, hereafter *LSL-mKate2*). The GEMM-ESC approach enables the rapid creation of mouse cancer models without the need for extensive intercrossing to generate appropriate genotypes, which is particularly important when modeling multiple new genetic modifications that may take many years to breed (11,13,14) (Fig. 1A). Alleles derived from GEMM-ESC can be outcrossed from the founder generation to establish independent strains.

We first designed an sgRNA overlapping codons 12 and 13 of *Kras* and 140mer single-stranded DNA (ssDNA) HDR templates carrying specific mutations (Fig. 1B), and introduced them into ESCs by nucleofection. For screening and genotyping purposes, each ssDNA template was designed to carry silent mutations that generate a unique restriction site adjacent to the specific codon change (Fig. 1B). Analysis of the bulk transfected population revealed efficient generation of indels in both the *LSL-G12D* and *wildtype Kras* alleles, suggesting that the single mismatch between the sgRNA and target region in *WT Kras* was not sufficient to dictate allele selectivity (Fig. 1C, Supplementary Fig. S1A). Indeed, every clone we identified that carried the desired HDR event on the *LSL* allele, carried an indel in the *WT* coding sequence (14/14 clones sequenced). Our follow-up efforts to first introduce silent mutations in the *WT* allele and then retarget the $Kras^{LSL\text{-}G12D}$ site also failed due to the introduction of indels in *Nras* with the *Kras WT*-specific sgRNA (Supplementary Fig. S1B–D).

During the course of this work, we independently developed an expression-optimized high-fidelity Cas9 variant that enabled selective and potent genome targeting (15,16). We thus tested whether this would provide the specificity required for selective *LSL-Kras* targeting. In contrast to what we observed following transfection of wildtype Cas9, expression of the optimized HF1 enzyme resulted in the generation of both indels and HDR integration in the *LSL* allele, but induced no detectable modifications in *WT Kras* (Fig. 1C, Supplementary Fig. S2A). Though we noted an overall decrease in the efficiency of HDR-targeting in comparison with *wildtype* Cas9 (5% vs 21%), the increased specificity allowed the identification of numerous clones carrying the desired targeting event (Supplementary Table S1). Targeted deep sequencing of *Kras* exon 2 revealed a consistent 5–6% HDR frequency, though the number of individual positive clones identified following each transfection varied from 1–5%, due to random clone selection (Supplementary Table S1). Clones identified to carry integration of the donor template by restriction digest were confirmed by allele specific PCR and direct Sanger sequencing (Fig. 1D, Supplementary Fig. S2B).

To determine the impact of selective KRAS mutational variants on cell and tumor biology, we chose to generate mice from three *LSL-Kras* genotypes: $Kras^{LSL\text{-}G12C}$, $Kras^{LSL\text{-}G12R}$, and $Kras^{LSL\text{-}G13D}$, as these mutations represent frequent and tissue-restricted mutational events in human colorectal cancer (CRC), pancreatic (PDAC), and lung (LUAD) respectively (Fig. 1E). To confirm that CRISPR-mediated HDR-targeting had not caused widespread mutagenesis or large-scale chromosome aberrations, we performed whole-exome sequencing (WES) on targeted ESC clones, those transfected with only the expression-optimized HF1 Cas9 variant (no sgRNA), or mock transfected cells (PAR). Consistent with highly selective targeting of the *Kras* locus by this sgRNA, we observed no differences in the number of *de novo* mutations (average 13.5 mutations/clone) in either PAR or HF1-only transfected clones, and those transfected with both HF1, sgRNA and HDR template (Supplementary Fig. S3A, Supplementary Table S2); In fact, the number of unique single nucleotide mutations detected in each clone was in line with the expected baseline mutation rate predicted in mouse ESCs (13.5/clone observed vs 10.4/clone estimated). (See methods for details; (17)). Moreover, most mutations were single nucleotide variants, rather than indels usually associated with Cas9-mediated mutagenesis, further suggesting they arose spontaneously during ESC culture. We did not detect any chromosome copy number alterations in targeted clones, with the exception of one $Kras^{LSL\text{-}G13D}$ clone, that showed a small deletion on chromosome 4 (Supplementary Fig. S3B); this clone was not used for mouse generation.

To produce mice, targeted $Kras^{LSL\text{-}mut}$ ESC clones were injected into host albino C57Bl/6J blastocysts, creating a range of high contribution chimeras (Supplementary Fig. S3C); we further bred the founders to C57Bl/6N mice to increase the number of animals for this study. To first confirm that each of the new strains showed equivalent expression of the *Kras* mutant allele, we generated multiple independent murine embryonic fibroblasts (MEFs) cultures from each $Kras^{LSL\text{-}mut}$ line (n=3) and immortalized the cells by disruption of p53 with CRISPR. Delivery of Cre recombinase on the same vector as Cas9 (Cas9-P2A-Cre) enabled simultaneous induction of each $Kras^{mut}$ allele. As expected, all mutant alleles were expressed similarly, as measured by allele-specific transcript reads counts (Fig. 1F) or total KRAS protein (Supplementary Fig. S3D). Consistent with previous analysis of $KRAS^{G12D}$ MEFs (18), induction of endogenous KRAS mutations in p53 *wildtype* cells led to a proliferative advantage, but there was no consistent difference in proliferation over 3 weeks between MEFs carrying each different KRAS mutant allele (Fig. 1G). RNAseq analysis in $Kras^{mut/Trp53^{KO}}$ MEFs (hereafter $KRAS^{MUT}$), revealed a range of transcriptional changes between WT and mutant cells, including the up and down regulation of genes previously linked to KRAS-driven transformation in murine fibroblasts (Fig. 1H, Supplementary Table S3) (19). Notably, though each of the KRAS variants carried the mutant transcriptional signature, the magnitude of the effect was markedly reduced in $KRAS^{G12R}$ and $KRAS^{G13D}$ cells (Fig. 1H). Ras-GTP levels were increased in all KRAS mutant MEFs, most elevated in $KRAS^{G12D}$ and $KRAS^{G12C}$, and lower in $KRAS^{G12R}$ and $KRAS^{G13D}$ cells (Fig. 1I). In low serum culture conditions, only $KRAS^{G12D}$ MEFs displayed clear activation of the downstream signaling effectors MEK/ERK/AKT, while $KRAS^{G12C}$ and $KRAS^{G13D}$ cells showed a lower level of pMEK/pERK than $KRAS^{G12D}$, but elevated above $KRAS^{WT}$ cells. $KRAS^{G12R}$ MEFs showed pMEK/pERK levels similar to $KRAS^{WT}$ cultures. All genotypes

showed similar phosphorylation of AKT and S6, with the exception of KRAS^{G12R} expressing MEFs, which had reduced pAKT and pS6, even below that of KRAS^{WT} cells. All MEFs remained responsive to upstream mitogenic signals, as acute EGF stimulation increased MEK, ERK, and AKT phosphorylation in all genotypes, including KRAS^{G12R} (Fig. 1I). Together, these data show that each *Kras$^{LSL\text{-}mut}$* strain enables comparable induction of endogenous *Kras$^{LSL\text{-}mut}$* alleles, and that while each mutation drives KRAS-associated phenotypes, the downstream effect of individual codon 12/13 KRAS mutations are not identical.

In vivo consequences of different Kras mutations in the colon and pancreas

To determine how distinct oncogenic alterations in codons 12/13 of KRAS impact tumor initiation *in vivo,* we built mouse models expressing each oncogenic *Kras* allele in the epithelium of the colon or pancreas. We chose these two organs as KRAS mutations occur in 40–50% of CRC cases, and are a near universal feature of PDAC, where KRAS mutations are considered the key disease-initiating event (14,20–22).

Previous work has demonstrated that induction of *Kras^{G12D}* mutations in the mouse colon epithelium drives widespread hyperplasia, characterized by lengthening of the crypts (23). To assess the impact of non-KRAS^{G12D} mutations on homeostasis of the colonic epithelium, we generated mice carrying each *Kras$^{LSL\text{-}mut}$* allele and *Fabp1-Cre* (24). In this model, Cre recombinase is expressed mid-gestation and activates KRAS^{MUT} in the colon and distal ileum (24). Consistent with published data, by 8 weeks of age colons expressing KRAS^{G12D} displayed widespread hyperplasia, showing significant thickening of the mucosa (Fig 2A–C, upper panel) (23,25). KRAS^{G12C} mutation induced a dramatic hyperplastic response, identical to that seen in KRAS^{G12D} colons, while colons expressing KRAS^{G13D} showed only moderate hyperplasia, as recently described (26). Strikingly, KRAS^{G12R} mutations had no obvious effect on crypt length or tissue structure, closely resembling KRAS^{WT} tissue (Fig. 2A–C). It is notable that of each of the four *Kras* mutations assessed here, *KRAS^{G12R}* is the least frequently observed in colon cancer. Despite the clear impact on crypt height (Fig. 2C), none of the KRAS mutations induced significant expansion the proliferative zone, quantified as the height of the region of BrdU incorporation (Fig. 2D). In contrast, G12D, G12C, and G13D mutant Kras colons all showed a significant expansion of KRT20-positive differentiated cells (Fig. 2E), together suggesting that increased crypt height may in part be due to persistence of committed epithelial cells. In all, these data show that just as mutation of different Ras family members has different effects on the colonic epithelium (23), subtle mutational changes within the same Ras gene (*Kras*) can dramatically alter the acute physiological response in an *in vivo* setting.

In the mouse pancreas, induction of KRAS^{G12D} or KRAS^{G12V} mutations in the developing epithelium drives transdifferentiation of the acinar compartment (acinar to ductal metaplasia; ADM) and the development of premalignant pancreatic intraepithelial neoplasias (PanINs) (21,22,27). We analyzed the impact of each different *Kras^{mut}* allele in a *Kras$^{LSL\text{-}mut}$/p48-Cre* (hereafter, *KC-MUT*) model whereby Cre is expressed mid-gestation and activates KRAS^{MUT} expression in almost all epithelial cells of the pancreas (14,28). These mice also carried a far-red mKate2 fluorescent reporter (29) to monitor Cre-mediated recombination

(Supplementary Fig. S4A). By 4 weeks of age, changes were apparent in the pancreas of all genotypes, with evidence of ADM and early PanIN development (Supplementary Fig. S4A). Transcriptome analysis of whole pancreatic tissue at this time revealed gene signatures consistent with KRAS activation in the pancreas, including upregulation of genes involved in epithelial to mesenchymal transition (EMT), KRAS signaling, and inflammatory responses (Supplementary Fig. S4B, Supplementary Table S4). Overall, altered gene sets were similar between all mutants at early this time-point (Supplementary Fig. S4B–C), though the increase in ductal (epithelial) and fibroblast markers, and corresponding decrease in the expression of genes marking acinar cells was higher in *KC-G12D* and *KC-G12C* pancreata, relative to *KC-G12R* and *KC-G13D* tissue (Supplementary Fig. S4D).

By 12 weeks of age, *KC-G12D* mice showed the expected appearance of PanIN lesions with loss of the acinar marker Carboxypeptidase A1 (CPA1), SOX9 induction (30), expression of the ductal lineage cytokeratin, KRT19, and the production of mucins (Alcian Blue) (Fig. 3A, Supplementary Fig. S5A–B). Accompanying this change was the infiltration of alpha smooth muscle actin (αSMA) positive stromal cells (αSMA; Fig. 3A) and ectopic deposition of extracellular matrix (Fig. 3A; Masson's Trichrome, blue staining). We quantified phenotypic change by measuring the relative area of normal acini, ADM, and PanINs across each genotype at 12 and 50–60 weeks of age (Fig. 3B, Supplementary Fig. S5B–D). As expected *KC-G12D* pancreata showed predominantly PanINs at 12 weeks (>90%), with little normal acinar tissue remaining. The overall PanIN burden was lower in *KC-G12C* mice (~50%), but the remainder of the pancreas was ADM, with less than 10% of pancreatic area containing normal acini (Fig. 3A, B). In contrast, at 12 weeks, *KC-G13D* pancreata appeared predominantly histologically normal, with less than one third of the pancreas showing evidence of ADM or PanIN transition (Fig. 3B); however, those regions containing PanINs closely resembled *KC-G12D* or *KC-G12C* lesions, containing increased Alcian blue and KRT19 staining (Fig. 3A). Similar to *KC-G12D* epithelium, *KC-G12R* lesions displayed early responses to *KRAS* activation, including elevated SOX9 expression (Supplementary Fig. S5A), but in contrast, showed almost no progression to PanIN (Fig. 3B, Supplementary Fig. S5C–D); *KC-G12R* pancreata had no evidence of Alcian Blue staining, while the epithelium showed expression of both acinar (CPA1) and ductal (KRT19) markers, suggesting a stalled progression at ADM (Fig. 3A,B). Lack of phenotypic progression was also evident in *KC-G12R* mice aged to 24 weeks and one year of age (Fig. 3B, Supplementary Fig. S6A–C), suggesting that the differences observed were not simply due to a moderate slowing of disease course. By contrast, *KC-G13D* mice showed more obvious time-dependent disease progression, and by 1 year, more than 50% of the pancreas was comprised of PanIN lesions.

At 12 weeks phospho-ERK was robustly detected in *KC-G12D* and *KC-G12C* pancreata, but was also more prominently associated with PanIN lesions that were more commonly found in these genotypes. In whole pancreas lysates at 4 weeks-of-age, ERK phosphorylation as well as Ras-GTP levels (Fig. 3C) were elevated in most strains compared to *KC-WT* tissue. In contrast to pERK, S6 phosphorylation was most strongly correlated with KRAS mutant ADM-like lesions, and thus was most apparent in *KC-G13D* and then in *KC-G12R* pancreas lysates (Fig. 3A,C). Together, these results show that $KRAS^{G12C}$, $KRAS^{G12R}$ and $KRAS^{G13D}$ mutations have reduced disease initiating capacity compared with the well-

studied KRAS^{G12D} mouse model in pancreas, and in some cases (G12R), do not follow the existing acini-ADM-PanIN progression model. It is worth noting that mice which did not carry the *Rosa26*-targeted *mKate2* reporter allele, *Kras$^{LSL\text{-}mut}$/p48-Cre* showed less penetrant ADM/PanIN phenotypes compared to those with mKate2 (Supplementary Fig. S7). The reason for this is not known but the data suggest an effect of the *rtTA3-IRES-mKate2* reporter or a *Rosa26*-linked phenotypic modifier. Importantly, this effect was seen across all genotypes (Supplementary Fig. S7), and in the case of *KC-G12R* and *KC-G13D* mice, dramatically reduced disease burden and pancreata more closely resembled KRAS^{WT} mice.

Acute pancreatitis promotes progression of KRAS^{G12C} and KRAS^{G13D}, but not KRAS^{G12R} preneoplastic lesions.

In patients, chronic pancreatitis substantially increases the risk of developing PDAC (31), and similarly, induction of acute pancreatitis in mice by high doses of the cholecystokinin (CCK) analogue, cerulein, promotes the early progression of disease (27,32,33). To determine whether acute pancreatitis would alter the progression of pancreatic precursors carrying different *Kras* mutations, we treated 9-week old mice with cerulein (8 doses, 50μg/kg, 1 hour apart), and assessed pancreatic response 20 days following injury (Fig. 4A). As expected, *Kras^{WT}* mice showed full recovery of the acinar tissue, while *KC-G12D* mice contained almost no normal acinar tissue, with the majority of the pancreas made up of PanIN lesions (Fig. 4B–C). Both *KC-G12C* and *KC-G13D* mice showed a marked progression of disease, with cerulein-treated *KC-G12C* pancreata containing more than 90% PanINs, while *KC-G13D* animals progressed from >65% normal acinar tissue, to >65% PanINs (Fig. 4B–C). Each of the cerulein-treated *KC-G12D, KC-G12C,* and *KC-G13D* mice showed a more severe histological phenotype than untreated mice, with evidence of inflamed areas, atrophy, and the presence of cysts (Fig. 4B). Strikingly, cerulein treated *KC-G12R* pancreata appeared similar to untreated *KC-G12R* mice, with the majority of tissue stalled at ADM, and less than 5% of the pancreas containing PanIN lesions (Fig. 4B–C).

Progression of KRAS^{G12D}-mutant preneoplastic lesions in the pancreas both before and following cerulein-induced pancreatitis requires the induction of a quiescent stem cell population marked by expression of Doublecortin-like kinase 1 (DCLK1) (34,35). To test whether KRAS^{G12R}- mutant pancreata had a selective defect in the induction of this stem population, we quantified the frequency of DCLK1-positive cells in untreated and cerulein-treated pancreata. Like *KC-G12D,* both *KC-G12C* and *KC-G13D* pancreata showed relatively abundant DCLK1-positive cells that were increased ~2-fold following cerulein treatment (Fig. 4D–E). In contrast, *KC-G12R* pancreata contained almost no DCLK1-positive cells, and while the number increased following pancreatitis, it remained lower than all other genotypes (Fig. 4D–E). Together, these data show that distinct *Kras* mutations have both a quantitative and qualitative impact on the pre-malignant transformation of the pancreatic epithelium. The specific failure of *KC-G12R* mutant pancreatic epithelium to transition from metaplastic acini to PanIN lesions is unexpected, given the frequency of *KRAS^{G12R}* mutation in human pancreatic cancer, but maybe linked to a reduction in the DCLK1-positive regenerative stem cells that are important for disease progression in the pancreas (34).

Generation and analysis of KP organoid models

To assess tumor-cell intrinsic differences between *Kras* mutations and explore the potential for these new strains as effective tools for testing therapeutic interventions, we derived ductal pancreatic organoids from each $Kras^{LSL\text{-}mut}$ mouse and induced simultaneous Cre-mediated KRAS activation and p53 disruption by CRISPR (hereafter, *KP-MUT*) (Fig. 5A). Targeted deep sequencing of the *Trp53* locus following Nutlin3 selection confirmed frameshift alterations in greater than 99.9% of all polyclonal organoid cultures (Supplementary Fig. S8A–B). We analyzed the transcriptional profile of each *KP-MUT* line compared to *KP-WT* organoids and identified a range of pathways activated in KRAS mutant cells (Supplementary Table S5), including MYC, p53 and AKT/MTOR signaling. In general, *KP-G12R* organoids showed less prominent KRAS transcriptional signatures (Fig. 5B), and a notable impairment of PI3K / AKT / mTORC1 signaling (Fig. 5B), consistent with recent reports in $KRAS^{G12R}$ mutant human PDAC cell lines (8). Similar to MEFs, RAS-GTP levels were elevated in all mutants, though moderately lower in *KP-G13D* organoids (Fig. 5C).

Pancreatic organoids from KPC tumors have been extensively characterized and reflect an accurate *ex vivo* surrogate for murine PDAC (35). Our *KP-MUT* organoids were generated *ex vivo*, from otherwise WT pancreatic ductal epithelium. To define the tumorigenic potential of the distinct *KP-MUT* models we transplanted organoids from each genotype by direct orthotopic injection into the pancreas of recipient ($Foxn1^{nu/nu}$) mice. For each genotype we combined two independent organoid lines (1:1) to ensure that any lack of tumor growth was not simply due to an isolated effect in one biological replicate. As expected, *KP-G12D* and *KP-G12C* organoids formed tumors in 9/10 injected animals (5/5 and 4/5, respectively), each showing variability in tumor size at 8 weeks (Fig. 5D–E). In contrast to the defect in early stage progression of pre-malignant lesions, but consistent with the observed frequency in human PDAC (2), *KP-G12R* organoids formed tumors in 5/5 injected animals, while no *KP-G13D* lines showed evidence of tumor growth (Fig. 5D–E). Together, these data suggest the pancreatic KP organoids lines represent a valuable pre-clinical platform to interrogate KRAS biology and possible therapeutic strategies.

G13D mutant organoids are sensitive to EGFR inhibition

Current clinical guidelines exclude all patients with *KRAS* mutant tumors from treatment with small molecules or antibodies that target the epidermal growth factor receptor (EGFR). However, retrospective clinical data (6,7) and cell line analyses (36,37) have suggested that colorectal cancers carrying $KRAS^{G13D}$ mutations may be sensitive to the EGFR-targeted antibody Cetuximab. While $KRAS^{G13D}$ mutations are infrequent in PDAC, we decided to ask whether a similar genotype-phenotype relationship would hold true in pancreatic organoids. Cetuximab does not recognize mouse EGFR, so we treated *KP-MUT* organoids with the cross-reactive small molecule EGFR inhibitor, Gefitinib. While *KP-G12D* organoids showed an acute molecular response to Gefitinib treatment, including decreased phosphorylation of downstream effectors ERK1/2 and AKT (Fig. 5F), and reduced EdU incorporation at high doses (Fig. 5G), they could be maintained over multiple passages in the presence of drug (Fig. 5H). In contrast, *KP-G13D* organoids showed a profound cell cycle arrest within 48 hours of Gefitinib treatment (Fig. 5G), even at intermediate doses, and

could not survive long-term (>1 week) drug exposure (Fig. 5H). *KP-G12C* and *KP-G12R* organoids, had an intermediate response to Gefitinib, but ultimately were able to maintain growth and proliferation with extended treatment (Supplementary Fig. S9A–B).

The response of $KRAS^{G13D}$ mutant cells to EGFR inhibition implies that they rely on additional pathway activation to achieve robust downstream mitogenic signaling. While KRAS mutations are rarely observed with other MAPK activating alterations, such as mutational activation of EGFR (38) or loss of negative regulators like Neurofibromin 1 (NF1) (39) (Supplementary Fig. S10A–B), recent work has identified a subset of BRAF mutations (Class III) that require upstream RAS signaling to induce high levels of MAPK activation. Interestingly, Class III BRAF mutations often co-occur with other RAS-MAPK mutations (39). Similarly, our analysis of more than 55,000 cancers in the Project Genie database (40) shows that tumors carrying KRAS codon 13 mutations are four times more likely to have additional driver mutations in MAPK genes (Supplementary Fig. S10B). In particular, $KRAS^{G13D}$ or $KRAS^{G13C}$ mutant cancers showed 5-fold enrichment in truncating NF1 mutations (Supplementary Fig. S10B), suggesting that these mutant proteins may be subject to upstream RTK/RAS and/or NF1 regulation.

To test this hypothesis directly we silenced NF1 in *KP-G12D* and *KP-G13D* pancreatic organoids using lentiviral- transduced miRNA-based shRNAs (Fig. 5I) and treated them with Gefitinib for 3 days (Fig. 5J). KP-G13D organoids transduced with a control shRNA (shRen.713) remained sensitive to EGFR inhibition while NF1-silenced organoids showed elevated pERK and continued expansion in the presence of drug (Fig. 5J–K). As expected, *KP-G12D* organoids showed no change in growth following EGFR inhibition, regardless NF1 expression (Fig. 5J).

EGFR inhibition reveals sensitivity to direct KRAS G12C inhibition

The recent development of covalent inhibitors of $KRAS^{G12C}$ represents the first strategy to directly target oncogenic KRAS, and multiple small molecules have shown promise in early stage clinical trials (41,42). To determine whether our $Kras^{LSL\text{-}G12C}$ model is an effective pre-clinical tool to investigate response and resistance to clinical KRAS G12C inhibitors, we treated *KP-MUT* organoids with ARS1620 - a selective $KRAS^{G12C}$ inhibitor that covalently binds to Cys12 when KRAS is in its GDP-bound inactive state (43). Surprisingly, *KP-G12C* organoids were completely insensitive to treatment with the KRAS G12C inhibitor alone, having no effect on morphology (Fig. 6A), proliferation (Fig. 6B), or organoid size (Fig. 6C, Supplementary Fig. S11). While ARS1620 reduced RAS-GTP levels selectively in KP-G12C and not KP-G12D organoids (Fig. 6D), it did not have a major impact on downstream signaling (Fig. 6E), perhaps due to endogenous receptor-mediated pathway activation. Consistent with a role for upstream mitogen signaling driving resistance to G12C inhibition, combined treatment with Gefitinib induced a further reduction in RAS-GTP levels (Fig. 6D), a profound block in proliferation within 48 hours (Fig. 6B), and eliminated all organoids within 6 days of treatment (Fig. 6A–C). These data indicate that upstream signaling by RTKs can impact the outcome of downstream KRAS G12C inhibition, in line with recent reports in cell lines and PDX models (42,44,45). Together, these findings highlight the

fidelity of which the *Kras*$^{LSL\text{-}G13D}$ and *Kras*$^{LSL\text{-}G12C}$ alleles recapitulate key signaling and feedback regulation observed in human cancer cells.

DISCUSSION

Mutant KRAS is a clear driver of human cancer and consequently there are numerous approved and investigational drugs in clinical use that target KRAS or upstream/downstream signaling mediators. Owing to expansive tumor sequencing efforts, we now know the types and frequency of *KRAS* alterations in different cancer types in great detail. In contrast, exactly how each distinct *KRAS* mutation impacts disease initiation and progression remains largely unknown. Defining the similarities and differences in cancer-associated KRAS mutations may reveal unique dependencies that can be exploited therapeutically. Here, we report the CRISPR-mediated generation of a series of new conditional *Kras*$^{LSL\text{-}mut}$ mouse models that recapitulate the tissue restricted alterations seen in human colorectal, pancreas, and lung cancers. Using these new pre-clinical tools, we show that subtle changes in mutations at codon 12 and 13 have a dramatic impact on tumor initiation and pre-malignant progression in the colon and pancreas, and that pancreas derived organoids carrying particular Kras alterations are differentially sensitive to targeted therapies.

The biochemical properties of individual KRAS mutant proteins have been well-characterized in *in vitro* systems, and show specific differences in intrinsic or GAP-mediated GTP hydrolysis and/or nucleotide exchange (4). The phenotypic consequences for each mutation have been much more difficult to define. Recently, Winters *et al* used a multiplexed adeno-associated virus (AAV) approach to engineer endogenous *Kras* mutations in the lung and pancreas of recipient mice (46). These experiments concluded that, in multiple sensitized backgrounds, KRAS^{G12D}, KRAS^{G12R}, and KRAS^{G13R} mutations readily induce tumor growth, while KRAS^{G12C} is a comparatively weak transforming allele. Our data assessing pre-malignant transformation in the colon and pancreas, and in KP organoids, and MEFs, suggest that KRAS^{G12C} is quite a potent KRAS mutant, while KRAS^{G12R} drives a less robust KRAS phenotype. There are notable differences between these studies, including the timing of Kras activation, presence/absence of co-altered tumor suppressors, and tissue context. One important technical consideration that may have relevant biological consequences is that using CRISPR-based HDR to engineer Kras mutations, Winters *et al*, invariably introduced disruptive mutations in the second *Kras* WT allele (46), as we observed during the first iteration of targeting ES cells. Whereas, our Cre-driven models retain the expression of WT KRAS. Indeed, in some contexts, WT KRAS acts as a tumor suppressor (47) and can influence the types of KRAS mutations that occur following chemical carcinogenesis (48). The role of WT KRAS protein is a poorly understood, but important question in cancer biology, as up to 50% of all KRAS mutant cancers show allelic imbalance involving amplification of the mutant gene, or loss of the wildtype copy (49). In this regard, our new mouse alleles offer a controlled setting to study the impact of WT Kras, by exploiting the silent mutations introduced to the mutant alleles (Fig. 1B) and selectively targeting the WT allele by CRISPR or RNAi-based strategies.

We show that subtle mutational differences in KRAS can dramatically alter the acute cellular response in an *in vivo* setting in multiple tissues. We noted striking differences among

KRAS mutants in the hyperplastic response of the colonic epithelium as well as early transformation steps of the pancreatic acini. In particular, $KRAS^{G12R}$ mutations had no measurable effect in the colon, and caused a partial acinar-to-ductal transition in the pancreas, but was unable to induce PanIN transformation. Even in the presence of inflammatory stimuli during acute pancreatitis, G12R mutants failed to induce obvious progression to PanINs. $KRAS^{G12R}$ pancreata showed a significantly reduced frequency of $DCLK1^{+}$ progenitor cells that have been linked to pancreatic cell transformation (34). This reduction in a known disease-initiating cell population may underlie the unusual difference observed in G12R mutants, but it remains unclear whether this is a cause or consequence of the stalled transition.

The observation that $KRAS^{G12R}$ mutants show differences in the early steps of pre-malignant progression in the pancreas is surprising given the relatively high frequency of $KRAS^{G12R}$ mutations in human PDAC. However, despite the atypical primary response to $KRAS^{G12R}$ induction, $KRAS^{G12R}$ mutations, but not $KRAS^{G13D}$ mutations, were sufficient to drive tumor growth in orthotopically transplanted pancreatic organoids in the absence of p53. This suggests that $Kras^{G12R}$ is a potent oncogenic allele in PDAC, but the cellular response to this event is context dependent. So, what could explain the altered progression in the pre-malignant state? First, the vast majority of our understanding of pancreatic cancer initiation has been driven by studies in the $Kras^{LSL\text{-}G12D}$ mouse and it is possible that not all KRAS mutants take the same path through tumor initiation. Second, it is also possible that the $KRAS^{G12R}$ mutant cells lack a key signal to drive PanIN development. While $KRAS^{G12R}$ lesions appear to have less ERK42/44 phosphorylation, this is more likely linked to the lack of ductal cells where pERK is highest (Fig. 2). Hobbs *et al*, recently revealed that $KRAS^{G12R}$ mutant cells have reduced AKT/PI3K activation and macropinocytosis (8). Both PI3K signaling and macropinocytosis have been directly linked to tumor initiation and/or progression in KRAS-driven pancreas cancer (50–52), providing a potential mechanism for this atypical *in vivo* response. Indeed, we noted diminished AKT phosphorylation and lower PI3K/AKT/MTOR transcriptional signatures in $KRAS^{G12R}$ mutant MEFs and organoids (Figures 1 & 5). This was less obvious in whole pancreas lysates, and perhaps indicates a need for more focused, dynamic, and epithelial-cell specific investigation of the *in vivo* response. As has been described for $KRAS^{G12D}$ models, disruption of p53 enabled tumorigenic progression of $KRAS^{G12R}$ mutant cells though it is unclear whether p53 is involved in the altered initial response of $KRAS^{G12R}$ mutant cells *in situ*. Whatever the underlying cause of restricted progression to the ductal state in $Kras^{LSL\text{-}G12R}$ mice, it is important to note that organoid culture conditions select for ductal-like cells, thus bypassing the stalled metaplastic progression observed in *KC-G12R* mice. As is clear from the data presented here, furthering our understanding of KRAS biology will require consideration of not only the specific oncogenic KRAS mutation, but also the cell context (cells vs. organoids vs. tissue) as well as co-occurring genetic alterations. These qualitative and quantitative differences in each setting will make it difficult to extrapolate general principles from any single experimental system.

To explore the utility of the $Kras^{LSL\text{-}mut}$ strains as pre-clinical tools, we generated KP pancreatic organoids and systematically tested two different targeted therapies. The response of $KRAS^{G13D}$ mutants to EGFR inhibiton that we observed in pancreatic organoids (Fig. 5)

is consistent with retrospective clinical data in colorectal cancer (6,7), and two recent publications using cancer cell lines (36,37). Similarly, these studies, like ours, show that NF1 is an important regulator of MAPK signaling output in $KRAS^{G13D}$ mutant cells, though the exact mechanism remains controversial. These observations parallel similar findings in BRAF mutant cells, where Rosen and colleagues identified distinct classes of oncogenic BRAF mutations based on their signaling dependencies (39). Class III BRAF mutations, like $KRAS^{G13D}$ mutations more frequently co-occur with mutations in additional MAPK pathway genes, and human cancers carrying these alterations are more sensitive to EGFR inhibition (53). Similarly, $KRAS^{A146T}$ mutations commonly co-occur with MAPK pathway mutations in CRC, and Poulin *et al* recently showed using a similar Cre-conditional *Kras* approach, that $KRAS^{A146T}$ mutations are poorly transforming in the colon and pancreas, like $KRAS^{G13D}$ (25,26). It is possible that the low oncogenicity of $KRAS^{G13D}$ mutations in the pancreas may be driven by an increased reliance on EGFR-mediated signaling, which has a dose-dependent impact on PDAC development, even in the presence of p53 mutations (54,55). Together, mutations such as $KRAS^{G13D}$ and $KRAS^{A146T}$ likely represent a distinct class of KRAS alterations that exert differential oncogenic effects and may confer sensitivity to existing clinical therapies.

Finally, we show that KP organoids carrying an endogenous $KRAS^{G12C}$ mutation are sensitive to a recently described covalent G12C inhibitor, but that response to this drug it is only effective in the presence of an EGFR inhibitor. Similar synergistic effects of G12C and EGFR inhibitors have been noted in human cancer cell lines (42,44,45), potentially due to reduced SOS-dependent GDP-GTP exchange, increasing the GDP-bound pool of $KRAS^{G12C}$ and rendering it more vulnerable to covalent modification (43,44,56). It may also be possible that the presence of WT KRAS in these cells allows escape from targeted G12C inhibition, and that this activity is RTK dependent. Further work in genetically defined systems such as these will provide a complete picture of the signaling and phenotypic consequences of clinical KRAS-G12C inhibitors, to further guide clinical application of these exciting small molecules.

Together these data describe the development of three new broadly useful precision oncology models, and highlight unique downstream consequences of subtle and cancer-relevant changes in KRAS mutations. The models faithfully represent the signaling dynamics and therapeutic response of human cancer cells and we expect they will serve as valuable immunocompetent pre-clinical tools to understand KRAS biology and develop more effective treatment strategies for KRAS-driven cancers.

METHODS

Cloning

VP12 vector expressing spCas9-HF1 (15) was codon optimized (16) and renamed HF1*. Sequences encoding Kras sgRNAs (Supplementary Table S6) were cloned into BbsI site of pX458, VP12-U6 and pXHF1* vectors. P53c sgRNA (Supplementary Table S6) was cloned into BsmBI site of Lenti-Cas9-Cre (LCC) vector. For shRNA cloning NF1 and Renilla 713 shRNAs (Supplementary Table S6) were cloned into XhoI/EcoRI site of SGEN vector (57).

ESC targeting

The p48 embryonic stem cell (ESC) line, derived previously as described somewhere else (14), was used to generate the new conditional LSL-Kras strains. ESC were cultured in KOSR + 2i media (58) on irradiated mouse embryonic fibloblast (MEF) feeder layers. 2×10^5 cells were co-transfected with 2ug of the Cas9/sgRNA vector PxHFc and 4 ul of ssODN HDR template (20 uM) using a Lonza X Unit Nucleofector with P3 buffer kit (Lonza #V4XP-3032). Four days following transfection, cells were plated at low density (500 cells) to enable clonal growth and the remaining culture was used to assess targeting efficiency from bulk population (see methods below). Clones were picked when they were visible without microscope. PCR amplification following digest to confirm template integration were carried out. Digested products were analyzed by QIAxcel (Qiagen). Positive clones were expanded and further validated by allele specific PCR and Sanger sequencing before sending them to perform blastocyst injection. *Estimation of expected mutation frequency from published data:* Cervantes et al that calculated a mutation rate of ~8×10^{-8} mutations per cell, per generation (17). As genome size is 3×10^9 bp, we estimate 3.75 mutations per genome/cell division. It took approximately 5 weeks to target, clone, and expand cells for cryopreservation. Mouse ESCs double every 4–5 hours (59), approximately 5.3 generations/day. So, 35 days of culture x 5.3 generations/day = 185.5 generations. 185.5 generations x 3.75 mutations/cell/generation = **696 mutations/cell**. Because we performed whole exome sequence which covers ~1.5% of whole genome: 696 mutations/cell x 0.015 genome coverage = 10.4 mutations/clone.

Clone screening

Clones were picked and trypsinized. Half of the volume was mixed with 2x DNA lysis buffer (20 mM Tris, pH 8.8, 40 mM $(NH_4)_2SO_4$, 20 mM $MgCl_2$, 10%Triton X 100, proteinase K 800 ug/ml, β-ME) and incubated for 2 h at 55°C following 20 min at 95°C to inactivate the Proteinase K. The remaining half was resuspended in media and transferred to a 48 well plate already containing 500 ul of ESC media.

The region of interest was amplified using 1ul of the crude gDNA lysis in 16ul volume using Promega 2X PCR master mix. HDR targeting was confirmed in each clone by digesting for 2 h half of the PCR product (8 ul) with the specific restriction enzyme for each integrated template (Fig. 1B).

Genomic DNA isolation, and T7 assay

ESCs were lysed in genomic lysis buffer (10 mM Tris, pH 7.5, 10 mM EDTA, 0.5% SDS, and 400 μg/ml proteinase K) for at least 2 h at 55 °C. After proteinase K heat inactivation at 95 °C for 15 min, 0.5 volume of 5 M NaCl was added, and samples were centrifuged for 10 min at 15,000 r.p.m. Supernatants were mixed with one volume of isopropanol, and DNA precipitates were washed in 70% EtOH before resuspension in 10 mM Tris, pH 8.0. Cas9-induced mutations were detected using the T7 endonuclease I. Briefly, the target region surrounding the expected mutation site was PCR amplified using Herculase II (600675, Agilent Technologies). PCR products were column-purified (Qiagen) and subjected to a series of melt–anneal temperature cycles with annealing temperatures gradually lowered in

each successive cycle. T7 endonuclease I was then added to selectively digest heteroduplex DNA. Digest products were visualized on a 2.5% agarose gel.

DNA-library preparation and MiSeq

Deep sequencing was performed on Clones Cas9-only transfected or co-transfected alongside an HDR template and successfully having integrated it. Briefly, DNA-library preparation and sequencing reactions were conducted at GENEWIZ. A NEB NextUltra DNA Library Preparation kit was used according to the manufacturer's recommendations (Illumina). Adaptor-ligated DNA was indexed and enriched through limited-cycle PCR. The DNA library was validated with a TapeStation (Agilent) and was quantified with a Qubit 2.0 fluorometer. The DNA library was quantified through real-time PCR (Applied Biosystems). The DNA library was loaded on an Illumina MiSeq instrument according to the manufacturer's instructions (Illumina). Sequencing was performed with a 2 × 150 paired-end con-figuration. Image analysis and base calling were conducted in MiSeq Control Software on a MiSeq instrument and verified independently with a custom workflow in Geneious R11.

Virus production

For virus production, HEK293T cells (ATCC CRL-3216) were plated in a 10 cm plate and transfected 12 h later (at 95% confluence) with a prepared mix in DMEM (with no supplements) containing 15 μg of lentiviral backbone LCMCp53c (pLenti-U6-p53c-sgRNA-Cas9-p2A-Cre), 7.5 μg of PAX2, 3.75 μg of VSV-G, and 78 μl of polyethylenimine (1 mg/ml). 36 h after transfection, the medium was replaced with target cell collection medium, and supernatants were harvested every 8–12 h up to 72 h after transfection.

Animal Studies

Production of mice and all treatments described were approved by the Institutional Animal Care and Use Committee (IACUC) at Weill Cornell Medicine, under protocol number 2014–0038. ES cell–derived mice were produced by blastocyst injection, and animals were either maintained on a mixed C57B6/129 background for experimental breeding or back-crossed to C57BL/6N mice. All LSL-Kras strains are available from Jackson Labs (G12C: B6N.129S4-*Kras*^{em1Ldow}/J (#033068); G12R: B6N.129S4-*Kras*^{em2Ldow}/J (#033316); G13D: B6N.129S4-*Kras*^{em3Ldow}/J (#033317). Progeny of both sexes were used for experiments and were genotyped for specific alleles (Kras$^{LSL\text{-}G12D}$, Kras$^{LSL\text{-}G12C}$, Kras$^{LSL\text{-}G12R}$, Kras$^{LSL\text{-}G13D}$, Ptf1/p48-Cre, Rosa26-LSL-tdTomato, CAGS-LSL-RIK) using primers described in Supplementary Table S6 and protocols available at www.dowlab.org/Protocols. Production of mice and all treatments described were approved by the IACUC at Weill Cornell Medicine under protocol number 2014–0038. For experiments analyzing the colon, all mice were collected at 8 weeks of age and injected with BrdU (1mg/mouse) two hours prior to harvest by intraperitoneal injection. Fabp1-Cre and *Kras*$^{LSL\text{-}mut}$ age matched littermates were used as controls. To induce experimental pancreatitis 9-week-old mice were subjected to 8 intraperitoneal injections of cerulein (50μg/kg) once every 1 hour (60). Mice were monitored daily, and euthanized 20 days after the acute treatment.

MEFs

Kras$^{LSL\text{-}mut}$ */LSL-tdTomato* males were bred with C57BL/6N females. MEFs were derived from day 12.5–14.5 postcoitum embryos following previously described protocol (61). Cells were cultured and expanded for one passage in DMEM (Corning) supplemented with 10% (v/v) FBS, and frozen at passage 2.

MEF immortalization—MEFs were immortalized by using a vector encoding Cas9 and a p53c sgRNA, as well as Cre recombinase to be able to activate Kras. Cells were thawed and immediately transduced with viral supernatants (1:2) in the presence of polybrene (8 μg/μl). Two days after transduction cells were selected in Nutlin-3 (10 μM). Established MEF cell lines expressing different Kras mutants (G12D, G12C, G12R and G13D) or Kras^{WT} and *Trp53* loss, were consequently used to perform RNAseq and western blot analysis. For protein experiments MEFs were starved overnight (2% FBS DMEM medium) and then stimulated with EGF 20 ng/ml for 10 min (62). All MEF data were obtained using at least 3 independent MEFs/genotype.

Fluorescence competitive proliferation assays—MEFs were thawed and after one passage infected with adenovirus-Cre purchased from University of Iowa (5×10^7 plaque-forming units / 1×10^6 cells). One day after infection, the percentage of tdTomato-positive cells was measured by flow cytometry (Attune NxT Flow Cytometer, Thermo Scientific) and cells were mixed at define proportions with their respective parental cells. tdTomato fluorescence was then tracked every 5 days by flow cytometry.

Ras-GTP-Pull down—Ras-GTP levels were assessed by Active Ras Pull-Down and Detection Kit (Thermo Scientific, Cat#16117Y) using Raf-RBD fused to GST to bind active (GTP-bound) Ras. Protein lysates (300–500 μg) were incubated with 30 μL glutathione resin and GST protein binding domains for one hour at 4°C to capture active small GTPases according to the manufacturer's protocol. After washing, the bound GTPase was recovered by eluting the GST-fusion protein from the glutathione resin. The purified GTPase was detected by western blot using mouse monoclonal anti-KRAS provided by the Kit.

Murine Pancreatic Ductal Organoid Culture

Isolation of normal pancreatic ducts was done modifying previously described protocol (63). Briefly, pancreas was minced and washed in Hanks's Balanced Salt Solution (Corning), and then incubated for 30 min at 37°C with Collagenase V to release the ducts. After washing twice with DMEM/10% FBS media, ducts were resuspended in *basal media* [Advanced DMEM/F12 (Corning) containing 1% penicillin/streptomycin, 1% glutamine, 1.25 mM N-acetylcysteine (Sigma Aldrich A9165-SG) and B27 Supplement (Gibco)], and mixed 1:10 with factor reduced (GFR) Matrigel (BD Biosciences). Forty microliters of the resuspension was plated per well in a 48-well plate and placed in a 37°C incubator to polymerize for 10 minutes. To culture ductal pancreatic organoids the *basal media* described above was supplemented with 10 nM Gastrin (Sigma), 50 ng/ml EGF (Peprotech), 10% RSPO1-conditioned media, 100 ng/ml Noggin (Peprotech), 100 ng/ml FGF10 (Peprotech) and 10 mM Nicotinamide (Sigma). Note: Culture freshly isolated organoids in pancreatic organoid media (POM) containing 10 μM Rock inhibitor (Y2732) during 48–72 h. For subculture and

maintenance, media were changed on organoids every two days and they were passaged 1:3 every 5 days. To passage, the growth media was removed and the Matrigel was resuspended in cold basal media and transferred to a 15-mL Falcon tube. Organoids were mechanically disassociated using a P1000 and pipetting 40 times. Five milliliters of cold PBS were added to the tube and cells were then centrifuged at 1,200 rpm for 5 minutes and the supernatant was aspirated. Cells were then resuspended in GFR Matrigel and replated as above. For freezing, after spinning, the cells were resuspended in complete containing 10% FBS and 10% DMSO and stored in liquid nitrogen indefinitely.

Organoid Transduction

To generate KP organoids ($Kras^{mut}$/Trp53 loss), normal pancreatic organoids were cultured in *transduction media* [POM containing CHIR99021 (5 μM) and Y-27632 (10 μM)] for 2 days prior to transduction. Single-cell suspensions were produced by dissociating organoids with TrypLE Express (Invitrogen#12604) for 5 minutes at 37°C. After trypsinization, cell clusters were resuspended in 400 μl of *transduction media* containing concentrated lentiviral particles in the presence of polybrene (8 μg/μl) and transferred into a 48-well culture plate. The plate was centrifuged at 600 x g at 32°C for 60 minutes, followed by another 4-hour incubation at 37°C. Cell clusters were spun down and plated in Matrigel.

Orthotopic pancreatic organoid transplantation

Two different KP lines carrying the same Kras mutation (G12D or G12C or G12R or G13D) or Kras WT lines were culture over 3 days in basal media, then mix at 1:1 ratio and injected (total volume 25 ul: 12.5 ul organoid in basal media/12.5 ul Matrigel) in the pancreas of nude (Foxn1nu) mice.

Organoid drug treatment

Organoids were plated in 120 μL Matrigel (3 × 40 μL droplets) in one 12-well plate and cultured in *basal media* with either DMSO or Gefitinib (1μM) or ARS-1620 (1μM) or Gef/ARS combined. Organoids were passaged 1:3 every 72 h and then cultured again in DMSO, Gefitinib, ARS-1620 or Gef/ARS combination.

EdU Flow Cytometry and Imaging in Organoids

Organoid EdU flow cytometry was performed using the Click-iT Plus EdU Alexa Fluor 647 Flow Cytometry Assay Kit (Thermo Fisher Scientific, # C10634). Pancreatic organoids were first incubated with 10 μM EdU for 4 hours at 37°C. One well of a 12-well plate was broken up by pipetting vigorously 50 times in 1 mL PBS, then diluted in 5 mL of PBS. Cells were pelleted at 1,100 rpm x 4 minutes at 4°C, then resuspended in 50 μL TrypLE and incubated at 37°C for 5 minutes. Five milliliters of PBS were then added to inactivate the TrypLE, and cells were pelleted. Cells were resuspended in 250 μL of 1% BSA in PBS, transferred to a 1.7-mL tube, and then pelleted at 3,000 rpm x 4 minutes. Cells were then resuspended in 100 μL Click-iT fixative, and processed as instructed in the Click-iT Plus EdU protocol (starting with Step 4.3). Wash and reaction volumes were 250 μL.

RNA isolation, cDNA synthesis, and qPCR

To isolate RNA from MEFs and pancreatic organoids, we used TRIzol (Thermo Fisher Scientific, #15596018) according to the manufacturer's instructions, and contaminating DNA was removed by DNase treatment for 10 minutes and column purification (Qiagen RNeasy #74106). Pancreas tissue portion for RNA purification was consistently collected from the tail of the organ and immediately cut into smaller pieces and immersed in RNAlater stabilization solution (Thermo Fisher) and incubate at 4°C overnight before storing the sample at −80 °C until RNA extraction was performed. Samples were homogenized using a Tissue Master 125 (Omni) and RNA purified using the RNAeasy Kit (Qiagen).

RNA sequencing

Total RNA was isolated using Trizol, DNAse treated and purified using the RNeasy mini kit (Qiagen, Hilden, Germany). Following RNA isolation, total RNA integrity was checked using a 2100 Bioanalyzer (Agilent Technologies, Santa Clara, CA). RNA concentrations were measured using the NanoDrop system (Thermo Fisher Scientific, Inc., Waltham, MA). Preparation of RNA sample library and RNAseq were performed by the Genomics Core Laboratory at Weill Cornell Medicine. Messenger RNA was prepared using TruSeq Stranded mRNA Sample Library Preparation kit (Illumina, San Diego, CA), according to the manufacturer's instructions. The normalized cDNA libraries were pooled and sequenced on Illumina NextSeq500 sequencer with single-end 75 cycles.

RNAseq analysis

Raw FASTQ files were mapped to mouse reference GRCm38 using STAR two-pass alignment (v2.4.1d; default parameters) (64), and transcript abundance estimates were performed using Kallisto (65), aligned to the same (GRCm38) reference genome. Kallisto transcript count data for each sample was concatenated, and transcript per million (TPM) data was reported for each gene after mapping gene symbols to ensemble IDs using R packages, *"tximport", tximportData", "ensembldb",* and *"EnsDb.Mmusculus.v79"*. Differential gene expression was estimated using DESeq2 (66). For data visualization and gene ranking, log fold changes were adjusted using *lfcShrink* in DESeq2, to minimize the effect size of poorly expressed genes. GSEA analysis (v3.0) was performed on pre-ranked gene sets from differential expression between control and treated groups. We used R (v3.6.1) and R Studio (v1.2.1335) to create all visualizations, perform hierarchical clustering and principal component analysis. Volcano plots, heatmaps and other visualizations were produced using the software packages:

Enhanced Volcano (https://bioconductor.org/packages/devel/bioc/html/EnhancedVolcano.html) pheatmap (https://cran.r-project.org/web/packages/pheatmap/index.html) ggplot2 (https://cran.r-project.org/web/packages/ggplot2/index.html)

Whole exome sequencing

Each gDNA sample based on Qubit quantification are mechanically fragmented on a Covaris E220 focused ultrasonicator (Covaris, Woburn, MA, USA). Two hundred ng of sheared gDNA were used to perform end repair, A-tailing and adapter ligation with Agilent SureSelect XT (Agilent Technologies, Santa Clara, CA) library preparation kit following the

manufacturer instructions. Then, the libraries were captured using Agilent SureSelectXT Mouse All Exon probes and amplified. The quality and quantities of the final libraries were checked by Agilent 2100 Bioanalyzer and Invitrogen Qubit 4.0 Fluorometer (Thermo Fisher, Waltham, MA). Libraries were pooled at 8 samples per lane and sequenced on an Illumina HiSeq 4000 sequencer (Illumina Inc, San Diego, CA) at PE 2×100 cycles. Copy number alterations were identified and plotted using cnvkit (v0.9.6) and single nucleotide variant were called using MuTect2.

Protein Analysis

Whole pancreas samples were minced and lysed in 600 μl of RIPA buffer by homogenization on the TissueLyser II (Quiagen). Pancreatic organoids were grown in 120 μL of Matrigel in one well of a 12-well dish. Organoids were then recovered from the Matrigel using Cell Recovery Solution. Organoid pellets were lysed in 30 μL RIPA buffer. For MEFs, they were cultured in 6-well plates and lysed in 150 μl of RIPA buffer. Antibodies used for Western blot analysis were: anti-actin-HRP (Abcam #ab49900), anti-α-Tubulin (Millipore Sigma #CP06), anti-pERK 44/42 (Cell Signaling Technology #4370), anti-ERK 44/42 (Cell Signaling Technology #9107), anti-pAKT (ser 473) (Cell Signaling Technology #4060), anti-AKT (Cell Signaling Technology #4691), pMEK (Cell Signaling Technology #9154), MEK (Cell Signaling Technology #8727), pS6 (Cell Signaling Technology #4858), S6 (Cell Signaling Technology #2317), anti-NF1 (Cell Signaling Technology #14623).

Immunofluorescence and Immunohistochemistry

Tissue, fixed in freshly prepared 4% paraformaldehyde for 24 hours, was embedded in paraffin, and sectioned by IDEXX RADIL. Sections were rehydrated and unmasked (antigen retrieval) by heat treatment for 10 minutes in a pressure cooker in 10 mM Tris/1 mM EDTA buffer (pH 9) containing 0.05% Tween 20. For immunohistochemistry, sections were treated with 3% H_2O_2 for 10 min and blocked in TBS/0.1% Triton X-100 containing 1% BSA. For immunofluorescence, sections were not treated with peroxidase. Primary antibodies, incubated at 4°C overnight in blocking buffer, were: rabbit anti-Ck19 (1:400, Abcam #ab133496), rabbit anti-Dclk1 (1:400, Abcam #109029), goat anti-CPA1 (1:400, R&D Systems AF2765), rabbit anti-αSMA (1:400, Abcam #ab5694), rabbit anti-pERK 44/42 (1:1000, Cell Signaling Technology #9101), rabbit anti-pS6 (1:1000, Cell Signaling Technology #2211), rabbit anti-Sox9 (1:1000, Millipore #AB5535), rabbit anti-tRFP (1:2000, Evogren #AB233), rat anti-BRDU (1:200 #ab6326), rabbit anti-KRT20 (1:200, Cell Signaling Technology #13063). For immunohistochemistry, sections were incubated with anti-rabbit ImmPRESS HRP-conjugated secondary antibodies (Vector Laboratories, #MP7401) and chromagen development was performed using ImmPact DAB (Vector Laboratories, #SK4105). Stained slides were counterstained with Harris' hematoxylin and mounted with Mowiol mounting media. For immunofluorescent stains, secondary antibodies were applied in TBS for 1 h at room temperature in the dark, washed twice with TBS, counterstained for 5 min with DAPI and mounted in ProLong Gold (Life Technologies, #P36930). Secondary antibodies used were: donkey anti-rabbit 594 (1:500, Invitrogen #A21207), donkey anti-goat 488 (1:500, Invitrogen #A11055). Masson's Trichrome stainings were performed by IDEXX Radil. Images of fluorescent and IHC stained sections

were acquired on a Zeiss Axioscope Imager (chromogenic stains), Nikon Eclipse T1microscope (IF stains). Raw.tif files were processed using FIJI (Image J) and/or Photoshop (Adobe Systems, San Jose, CA, USA) to create stacks, adjust levels and/or apply false coloring. Crypt length and proliferative zone were quantified in FIJI (Image J) using the 'Measure' feature.

Data Availability

Raw exomeSeq and RNAseq data have been deposited in the sequence read archive (SRA) under accession PRJNA578549.

Supplementary Material

Refer to Web version on PubMed Central for supplementary material.

Acknowledgements

We thank Miguel Foronda for technical and experimental advice. This work was supported by a project grant from the National Cancer Institute (NIH/NCI) under award R01CA195787. We thank the Weill Cornell Genomics Resource Core Facility who performed library preparation and sequencing for WES and RNAseq. MPZ is supported in part by National Cancer Institute (NCI) Grant NIH T32 CA203702. The content is solely the responsibility of the authors and does not necessarily represent the official views of the NIH.

REFERENCES

1. Zehir A, Benayed R, Shah RH, Syed A, Middha S, Kim HR. et al. Mutational landscape of metastatic cancer revealed from prospective clinical sequencing of 10,000 patients. Nat Med 2017;23(6):703–13 doi 10.1038/nm.4333. [PubMed: 28481359]
2. Cerami E, Gao J, Dogrusoz U, Gross BE, Sumer SO, Aksoy BA. et al. The cBio cancer genomics portal: an open platform for exploring multidimensional cancer genomics data. Cancer Discov 2012;2(5):401–4 doi 10.1158/2159-8290.CD-12-0095. [PubMed: 22588877]
3. Temko D, Tomlinson IPM, Severini S, Schuster-Bockler B, Graham TA. The effects of mutational processes and selection on driver mutations across cancer types. Nat Commun 2018;9(1):1857 doi 10.1038/s41467-018-04208-6. [PubMed: 29748584]
4. Haigis KM. KRAS Alleles: The Devil Is in the Detail. Trends Cancer 2017;3(10):686–97 doi 10.1016/j.trecan.2017.08.006. [PubMed: 28958387]
5. Hunter JC, Manandhar A, Carrasco MA, Gurbani D, Gondi S, Westover KD. Biochemical and Structural Analysis of Common Cancer-Associated KRAS Mutations. Mol Cancer Res 2015;13(9):1325–35 doi 10.1158/1541-7786.MCR-15-0203. [PubMed: 26037647]
6. De Roock W, Jonker DJ, Di Nicolantonio F, Sartore-Bianchi A, Tu D, Siena S. et al. Association of KRAS p.G13D mutation with outcome in patients with chemotherapy-refractory metastatic colorectal cancer treated with cetuximab. Jama 2010;304(16):1812–20 doi 10.1001/jama.2010.1535. [PubMed: 20978259]
7. Tejpar S, Celik I, Schlichting M, Sartorius U, Bokemeyer C, Van Cutsem E. Association of KRAS G13D tumor mutations with outcome in patients with metastatic colorectal cancer treated with first-line chemotherapy with or without cetuximab. J Clin Oncol 2012;30(29):3570–7 doi 10.1200/JCO.2012.42.2592. [PubMed: 22734028]
8. Hobbs GA, Baker NM, Miermont AM, Thurman RD, Pierobon M, Tran TH. et al. Atypical KRAS(G12R) Mutant Is Impaired in PI3K Signaling and Macropinocytosis in Pancreatic Cancer. Cancer Discov 2020;10(1):104–23 doi 10.1158/2159-8290.CD-19-1006. [PubMed: 31649109]
9. Jackson EL, Willis N, Mercer K, Bronson RT, Crowley D, Montoya R. et al. Analysis of lung tumor initiation and progression using conditional expression of oncogenic K-ras. Genes Dev 2001;15(24):3243–8 doi 10.1101/gad.943001. [PubMed: 11751630]

10. Guerra C, Mijimolle N, Dhawahir A, Dubus P, Barradas M, Serrano M. et al. Tumor induction by an endogenous K-ras oncogene is highly dependent on cellular context. Cancer Cell 2003;4(2):111–20. [PubMed: 12957286]
11. Huijbers IJ, Del Bravo J, Bin Ali R, Pritchard C, Braumuller TM, van Miltenburg MH. et al. Using the GEMM-ESC strategy to study gene function in mouse models. Nat Protoc 2015;10(11):1755–85 doi 10.1038/nprot.2015.114. [PubMed: 26492136]
12. Huijbers IJ, Krimpenfort P, Berns A, Jonkers J. Rapid validation of cancer genes in chimeras derived from established genetically engineered mouse models. BioEssays : news and reviews in molecular, cellular and developmental biology 2011;33(9):701–10 doi 10.1002/bies.201100018.
13. Premsrirut PK, Dow LE, Kim SY, Camiolo M, Malone CD, Miething C. et al. A rapid and scalable system for studying gene function in mice using conditional RNA interference. Cell 2011;145(1):145–58 doi 10.1016/j.cell.2011.03.012. [PubMed: 21458673]
14. Saborowski M, Saborowski A, Morris JPt, Bosbach B, Dow LE, Pelletier J. et al. A modular and flexible ESC-based mouse model of pancreatic cancer. Genes & development 2014;28(1):85–97 doi 10.1101/gad.232082.113. [PubMed: 24395249]
15. Kleinstiver BP, Pattanayak V, Prew MS, Tsai SQ, Nguyen NT, Zheng Z. et al. High-fidelity CRISPR-Cas9 nucleases with no detectable genome-wide off-target effects. Nature 2016;529(7587):490–5 doi 10.1038/nature16526. [PubMed: 26735016]
16. Zafra MP, Schatoff EM, Katti A, Foronda M, Breinig M, Schweitzer AY. et al. Optimized base editors enable efficient editing in cells, organoids and mice. Nat Biotechnol 2018;36(9):888–93 doi 10.1038/nbt.4194. [PubMed: 29969439]
17. Cervantes RB, Stringer JR, Shao C, Tischfield JA, Stambrook PJ. Embryonic stem cells and somatic cells differ in mutation frequency and type. Proc Natl Acad Sci U S A 2002;99(6):3586–90 doi 10.1073/pnas.062527199. [PubMed: 11891338]
18. Tuveson DA, Shaw AT, Willis NA, Silver DP, Jackson EL, Chang S. et al. Endogenous oncogenic K-ras(G12D) stimulates proliferation and widespread neoplastic and developmental defects. Cancer Cell 2004;5(4):375–87. [PubMed: 15093544]
19. Chiaradonna F, Pirola Y, Ricciardiello F, Palorini R. Transcriptional profiling of immortalized and K-ras-transformed mouse fibroblasts upon PKA stimulation by forskolin in low glucose availability. Genom Data 2016;9:100–4 doi 10.1016/j.gdata.2016.07.004. [PubMed: 27486565]
20. Cancer Genome Atlas Research Network. Electronic address aadhe, Cancer Genome Atlas Research N. Integrated Genomic Characterization of Pancreatic Ductal Adenocarcinoma. Cancer Cell 2017;32(2):185–203 e13 doi 10.1016/j.ccell.2017.07.007.
21. Hingorani SR, Petricoin EF, Maitra A, Rajapakse V, King C, Jacobetz MA. et al. Preinvasive and invasive ductal pancreatic cancer and its early detection in the mouse. Cancer Cell 2003;4(6):437–50. [PubMed: 14706336]
22. Hingorani SR, Wang L, Multani AS, Combs C, Deramaudt TB, Hruban RH. et al. Trp53R172H and KrasG12D cooperate to promote chromosomal instability and widely metastatic pancreatic ductal adenocarcinoma in mice. Cancer Cell 2005;7(5):469–83 doi 10.1016/j.ccr.2005.04.023. [PubMed: 15894267]
23. Haigis KM, Kendall KR, Wang Y, Cheung A, Haigis MC, Glickman JN. et al. Differential effects of oncogenic K-Ras and N-Ras on proliferation, differentiation and tumor progression in the colon. Nat Genet 2008;40(5):600–8 doi 10.1038/ng.115. [PubMed: 18372904]
24. Saam JR, Gordon JI. Inducible gene knockouts in the small intestinal and colonic epithelium. J Biol Chem 1999;274(53):38071–82 doi 10.1074/jbc.274.53.38071. [PubMed: 10608876]
25. Poulin EJ, Bera AK, Lu J, Lin YJ, Strasser SD, Paulo JA. et al. Tissue-Specific Oncogenic Activity of KRAS(A146T). Cancer Discov 2019;9(6):738–55 doi 10.1158/2159-8290.CD-18-1220. [PubMed: 30952657]
26. Johnson CW, Lin YJ, Reid D, Parker J, Pavlopoulos S, Dischinger P. et al. Isoform-Specific Destabilization of the Active Site Reveals a Molecular Mechanism of Intrinsic Activation of KRas G13D. Cell Rep 2019;28(6):1538–50 e7 doi 10.1016/j.celrep.2019.07.026.
27. Guerra C, Schuhmacher AJ, Canamero M, Grippo PJ, Verdaguer L, Perez-Gallego L. et al. Chronic pancreatitis is essential for induction of pancreatic ductal adenocarcinoma by K-Ras oncogenes in adult mice. Cancer Cell 2007;11(3):291–302 doi 10.1016/j.ccr.2007.01.012. [PubMed: 17349585]

28. Kawaguchi Y, Cooper B, Gannon M, Ray M, MacDonald RJ, Wright CV. The role of the transcriptional regulator Ptf1a in converting intestinal to pancreatic progenitors. Nat Genet 2002;32(1):128–34 doi 10.1038/ng959. [PubMed: 12185368]
29. Dow LE, Nasr Z, Saborowski M, Ebbesen SH, Manchado E, Tasdemir N. et al. Conditional reverse tet-transactivator mouse strains for the efficient induction of TRE-regulated transgenes in mice. PLoS ONE 2014;9(4):e95236 doi 10.1371/journal.pone.0095236.
30. Kopp JL, Dubois CL, Schaffer AE, Hao E, Shih HP, Seymour PA. et al. Sox9+ ductal cells are multipotent progenitors throughout development but do not produce new endocrine cells in the normal or injured adult pancreas. Development 2011;138(4):653–65 doi 10.1242/dev.056499. [PubMed: 21266405]
31. Lowenfels AB, Maisonneuve P, Cavallini G, Ammann RW, Lankisch PG, Andersen JR. et al. Pancreatitis and the risk of pancreatic cancer. International Pancreatitis Study Group. N Engl J Med 1993;328(20):1433–7 doi 10.1056/NEJM199305203282001. [PubMed: 8479461]
32. Morris JPt Cano DA, Sekine S Wang SC, Hebrok M. Beta-catenin blocks Kras-dependent reprogramming of acini into pancreatic cancer precursor lesions in mice. J Clin Invest 2010;120(2):508–20 doi 10.1172/JCI40045. [PubMed: 20071774]
33. Carriere C, Young AL, Gunn JR, Longnecker DS, Korc M. Acute pancreatitis markedly accelerates pancreatic cancer progression in mice expressing oncogenic Kras. Biochem Biophys Res Commun 2009;382(3):561–5 doi 10.1016/j.bbrc.2009.03.068. [PubMed: 19292977]
34. Westphalen CB, Takemoto Y, Tanaka T, Macchini M, Jiang Z, Renz BW. et al. Dclk1 Defines Quiescent Pancreatic Progenitors that Promote Injury-Induced Regeneration and Tumorigenesis. Cell Stem Cell 2016;18(4):441–55 doi 10.1016/j.stem.2016.03.016. [PubMed: 27058937]
35. Boj SF, Hwang CI, Baker LA, Chio II, Engle DD, Corbo V. et al. Organoid models of human and mouse ductal pancreatic cancer. Cell 2015;160(1–2):324–38 doi 10.1016/j.cell.2014.12.021. [PubMed: 25557080]
36. McFall T, Diedrich JK, Mengistu M, Littlechild SL, Paskvan KV, Sisk-Hackworth L. et al. A systems mechanism for KRAS mutant allele-specific responses to targeted therapy. Sci Signal 2019;12(600) doi 10.1126/scisignal.aaw8288.
37. Rabara D, Tran TH, Dharmaiah S, Stephens RM, McCormick F, Simanshu DK. et al. KRAS G13D sensitivity to neurofibromin-mediated GTP hydrolysis. Proc Natl Acad Sci U S A 2019;116(44):22122–31 doi 10.1073/pnas.1908353116. [PubMed: 31611389]
38. Unni AM, Lockwood WW, Zejnullahu K, Lee-Lin SQ, Varmus H. Evidence that synthetic lethality underlies the mutual exclusivity of oncogenic KRAS and EGFR mutations in lung adenocarcinoma. Elife 2015;4:e06907 doi 10.7554/eLife.06907.
39. Yao Z, Yaeger R, Rodrik-Outmezguine VS, Tao A, Torres NM, Chang MT. et al. Tumours with class 3 BRAF mutants are sensitive to the inhibition of activated RAS. Nature 2017;548(7666):234–8 doi 10.1038/nature23291. [PubMed: 28783719]
40. Consortium APG. AACR Project GENIE: Powering Precision Medicine through an International Consortium. Cancer Discov 2017;7(8):818–31 doi 10.1158/2159-8290.CD-17-0151. [PubMed: 28572459]
41. Canon J, Rex K, Saiki AY, Mohr C, Cooke K, Bagal D. et al. The clinical KRAS(G12C) inhibitor AMG 510 drives anti-tumour immunity. Nature 2019;575(7781):217–23 doi 10.1038/s41586-019-1694-1. [PubMed: 31666701]
42. Hallin J, Engstrom LD, Hargis L, Calinisan A, Aranda R, Briere DM. et al. The KRAS(G12C) Inhibitor MRTX849 Provides Insight toward Therapeutic Susceptibility of KRAS-Mutant Cancers in Mouse Models and Patients. Cancer Discov 2020;10(1):54–71 doi 10.1158/2159-8290.CD-19-1167. [PubMed: 31658955]
43. Ostrem JM, Shokat KM. Direct small-molecule inhibitors of KRAS: from structural insights to mechanism-based design. Nature reviews 2016;15(11):771–85 doi 10.1038/nrd.2016.139.
44. Lito P, Solomon M, Li LS, Hansen R, Rosen N. Allele-specific inhibitors inactivate mutant KRAS G12C by a trapping mechanism. Science 2016;351(6273):604–8 doi 10.1126/science.aad6204. [PubMed: 26841430]

45. Misale S, Fatherree JP, Cortez E, Li C, Bilton S, Timonina D. et al. KRAS G12C NSCLC Models Are Sensitive to Direct Targeting of KRAS in Combination with PI3K Inhibition. Clin Cancer Res 2019;25(2):796–807 doi 10.1158/1078-0432.CCR-18-0368. [PubMed: 30327306]
46. Winters IP, Chiou SH, Paulk NK, McFarland CD, Lalgudi PV, Ma RK. et al. Multiplexed in vivo homology-directed repair and tumor barcoding enables parallel quantification of Kras variant oncogenicity. Nat Commun 2017;8(1):2053 doi 10.1038/s41467-017-01519-y. [PubMed: 29233960]
47. Zhang Z, Wang Y, Vikis HG, Johnson L, Liu G, Li J. et al. Wildtype Kras2 can inhibit lung carcinogenesis in mice. Nat Genet 2001;29(1):25–33 doi 10.1038/ng721. [PubMed: 11528387]
48. Westcott PM, Halliwill KD, To MD, Rashid M, Rust AG, Keane TM. et al. The mutational landscapes of genetic and chemical models of Kras-driven lung cancer. Nature 2015;517(7535):489–92 doi 10.1038/nature13898. [PubMed: 25363767]
49. Burgess MR, Hwang E, Mroue R, Bielski CM, Wandler AM, Huang BJ. et al. KRAS Allelic Imbalance Enhances Fitness and Modulates MAP Kinase Dependence in Cancer. Cell 2017;168(5):817–29 e15 doi 10.1016/j.cell.2017.01.020. [PubMed: 28215705]
50. Baer R, Cintas C, Dufresne M, Cassant-Sourdy S, Schonhuber N, Planque L. et al. Pancreatic cell plasticity and cancer initiation induced by oncogenic Kras is completely dependent on wild-type PI 3-kinase p110alpha. Genes Dev 2014;28(23):2621–35 doi 10.1101/gad.249409.114. [PubMed: 25452273]
51. Commisso C, Davidson SM, Soydaner-Azeloglu RG, Parker SJ, Kamphorst JJ, Hackett S. et al. Macropinocytosis of protein is an amino acid supply route in Ras-transformed cells. Nature 2013;497(7451):633–7 doi 10.1038/nature12138. [PubMed: 23665962]
52. Eser S, Reiff N, Messer M, Seidler B, Gottschalk K, Dobler M. et al. Selective requirement of PI3K/PDK1 signaling for Kras oncogene-driven pancreatic cell plasticity and cancer. Cancer Cell 2013;23(3):406–20 doi 10.1016/j.ccr.2013.01.023. [PubMed: 23453624]
53. Yaeger R, Chatila WK, Lipsyc MD, Hechtman JF, Cercek A, Sanchez-Vega F. et al. Clinical Sequencing Defines the Genomic Landscape of Metastatic Colorectal Cancer. Cancer Cell 2018;33(1):125–36 e3 doi 10.1016/j.ccell.2017.12.004. [PubMed: 29316426]
54. Ardito CM, Gruner BM, Takeuchi KK, Lubeseder-Martellato C, Teichmann N, Mazur PK. et al. EGF receptor is required for KRAS-induced pancreatic tumorigenesis. Cancer Cell 2012;22(3):304–17 doi 10.1016/j.ccr.2012.07.024. [PubMed: 22975374]
55. Navas C, Hernandez-Porras I, Schuhmacher AJ, Sibilia M, Guerra C, Barbacid M. EGF receptor signaling is essential for k-ras oncogene-driven pancreatic ductal adenocarcinoma. Cancer Cell 2012;22(3):318–30 doi 10.1016/j.ccr.2012.08.001. [PubMed: 22975375]
56. Ostrem JM, Peters U, Sos ML, Wells JA, Shokat KM. K-Ras(G12C) inhibitors allosterically control GTP affinity and effector interactions. Nature 2013;503(7477):548–51 doi 10.1038/nature12796. [PubMed: 24256730]
57. Fellmann C, Hoffmann T, Sridhar V, Hopfgartner B, Muhar M, Roth M. et al. An optimized microRNA backbone for effective single-copy RNAi. Cell Rep 2013;5(6):1704–13 doi 10.1016/j.celrep.2013.11.020. [PubMed: 24332856]
58. Gertsenstein M, Nutter LM, Reid T, Pereira M, Stanford WL, Rossant J. et al. Efficient generation of germ line transmitting chimeras from C57BL/6N ES cells by aggregation with outbred host embryos. PLoS One 2010;5(6):e11260 doi 10.1371/journal.pone.0011260.
59. Wang J, Alexander P, McKnight SL. Metabolic specialization of mouse embryonic stem cells. Cold Spring Harb Symp Quant Biol 2011;76:183–93 doi 10.1101/sqb.2011.76.010835. [PubMed: 22071264]
60. Devenyi ZJ, Orchard JL, Powers RE. Xanthine oxidase activity in mouse pancreas: effects of caerulein-induced acute pancreatitis. Biochem Biophys Res Commun 1987;149(3):841–5 doi 10.1016/0006-291x(87)90484-0. [PubMed: 3480708]
61. Brugarolas J, Bronson RT, Jacks T. p21 is a critical CDK2 regulator essential for proliferation control in Rb-deficient cells. J Cell Biol 1998;141(2):503–14 doi 10.1083/jcb.141.2.503. [PubMed: 9548727]

62. Stolze B, Reinhart S, Bulllinger L, Frohling S, Scholl C. Comparative analysis of KRAS codon 12, 13, 18, 61, and 117 mutations using human MCF10A isogenic cell lines. Sci Rep 2015;5:8535 doi 10.1038/srep08535. [PubMed: 25705018]

63. Huch M, Bonfanti P, Boj SF, Sato T, Loomans CJ, van de Wetering M. et al. Unlimited in vitro expansion of adult bi-potent pancreas progenitors through the Lgr5/R-spondin axis. EMBO J 2013;32(20):2708–21 doi 10.1038/emboj.2013.204. [PubMed: 24045232]

64. Dobin A, Davis CA, Schlesinger F, Drenkow J, Zaleski C, Jha S. et al. STAR: ultrafast universal RNA-seq aligner. Bioinformatics 2013;29(1):15–21 doi 10.1093/bioinformatics/bts635. [PubMed: 23104886]

65. Bray NL, Pimentel H, Melsted P, Pachter L. Near-optimal probabilistic RNA-seq quantification. Nat Biotechnol 2016;34(5):525–7 doi 10.1038/nbt.3519. [PubMed: 27043002]

66. Love MI, Huber W, Anders S. Moderated estimation of fold change and dispersion for RNA-seq data with DESeq2. Genome Biol 2014;15(12):550 doi 10.1186/s13059-014-0550-8. [PubMed: 25516281]

SIGNIFICANCE

KRAS is the most frequently mutated oncogene. Here, we describe new pre-clinical models that mimic tissue-selective KRAS mutations and show that each mutation has distinct cellular consequences *in vivo*, and carries differential sensitivity to targeted therapeutic agents.

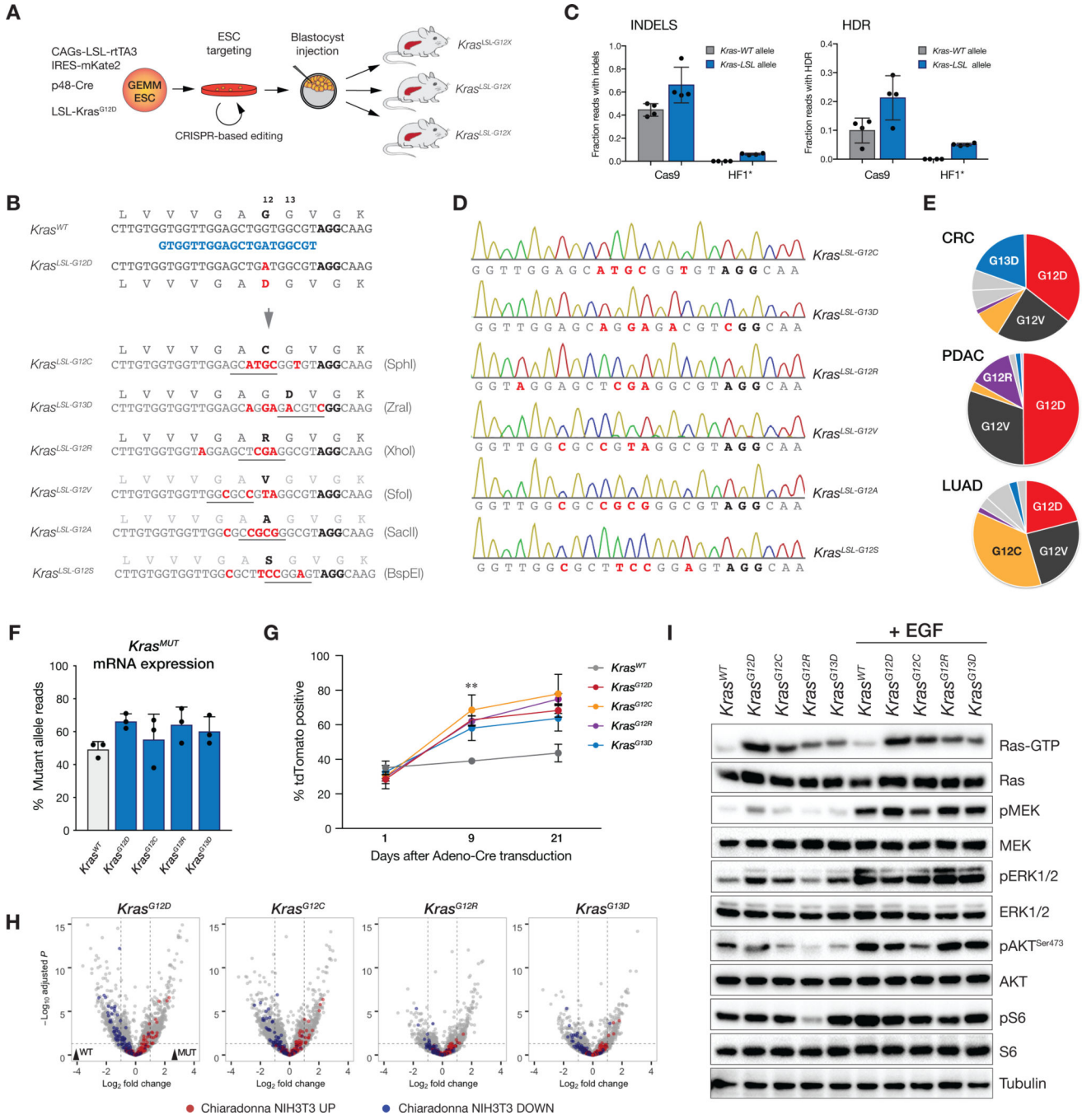

Figure 1. CRISPR strategy to generate new conditional Kras variants.

A. Schematic representation of the pipeline to generate the new LSL-Kras alleles in pancreatic GEMM-ESCs, carrying Kras$^{LSL\text{-}G12D}$, a pancreas specific Cre (p48-Cre) and far-red fluorescent reporter. **B.** Kras sgRNA (blue) aligned to WT and LSL alleles. Lower sequences represent the central 33bp of the single-stranded oligonucleotide (ssODN) HDR templates bearing each new mutation and unique restriction site. **C.** Targeted deep sequencing from bulk ESC population 3 days following transfection. Error bars are +/− SD, n=4 independent transfections. **D.** Sanger sequencing traces of the LSL allele from ESCs

clones carrying each Kras mutation. **E.** Pie charts representing the spectrum of codon 12 and 13 *KRAS* mutations in colorectal cancer (CRC), lung adenocarcinoma (LUAD) and pancreatic adenocarcinoma (PDAC). **F.** Percentage of mutant Kras mRNA reads in each Kras mutant murine embryonic fibroblast (MEF) lines, obtained RNAseq profiling. Percentage of allele specific WT reads obtained using a single nucleotide polymorphism (SNP) close to codon 12. Error bars are SD, n=3 independently generated MEF lines from each genotype. **G.** Fluorescence proliferation 'competition' assay in MEFs showing relative abundance of tdTomato-positive cells after AdenoCre transduction. Error bars are SD, n=3 independently generated MEF lines from each genotype, **p value < 0.01 between G12D/G12R vs WT at day 9 post infection. **H.** Volcano plots from MEF RNAseq data comparing all mutants with a published gene set Chiaradonna, 2016 #3072}, n=3 independently generated MEF lines from each genotype. **I**. Ras-GTP levels and activation of downstream signaling in $Kras^{Mut}$ or WT MEFs cultured in 0.5 % FBS medium upon stimulation with EGF (20 ng/ml) for 10 min. Results are representative of three similar experiments.

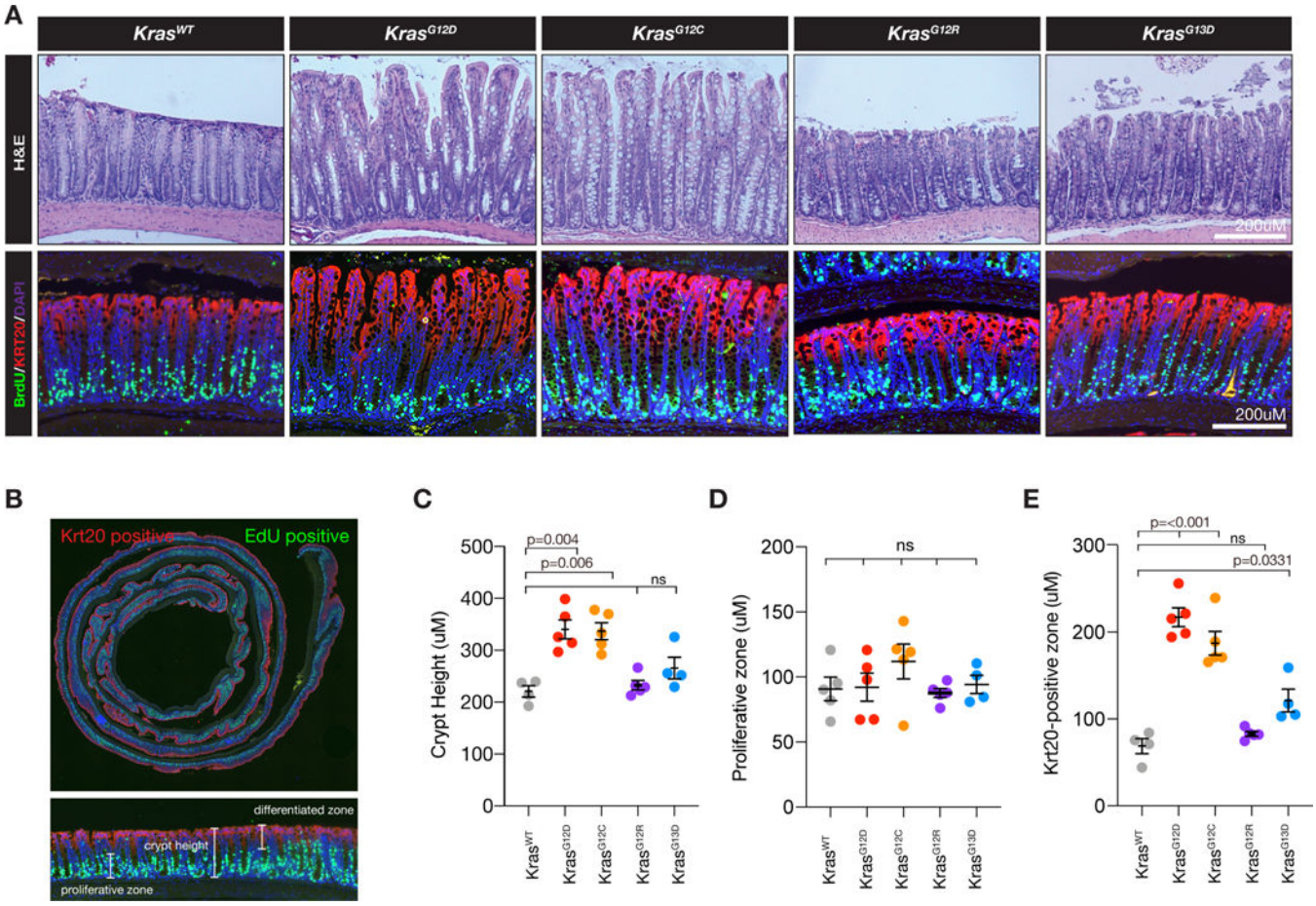

Figure 2. Colon specific phenotypes of Kras alleles.

A. Representative biological cross sections and immunofluorescent stains of colon epithelium from 8-week-old mice expressing different forms of mutant Kras as indicated. All groups express Cre under the Fabp1 promoter. **B**. Representative image from a swiss-roll of the colon from a *Kras*$^{LSL\text{-}G12D}$ mice. Scatter plots showing the average height of the colonic crypts (C), proliferative (BrdU-positive) zone (**D**), and differentiated (Krt20-positive) zone (**E**). Data are means +SEM of 2–5 mice per genotype, as indicated, 2-way ANOVA.

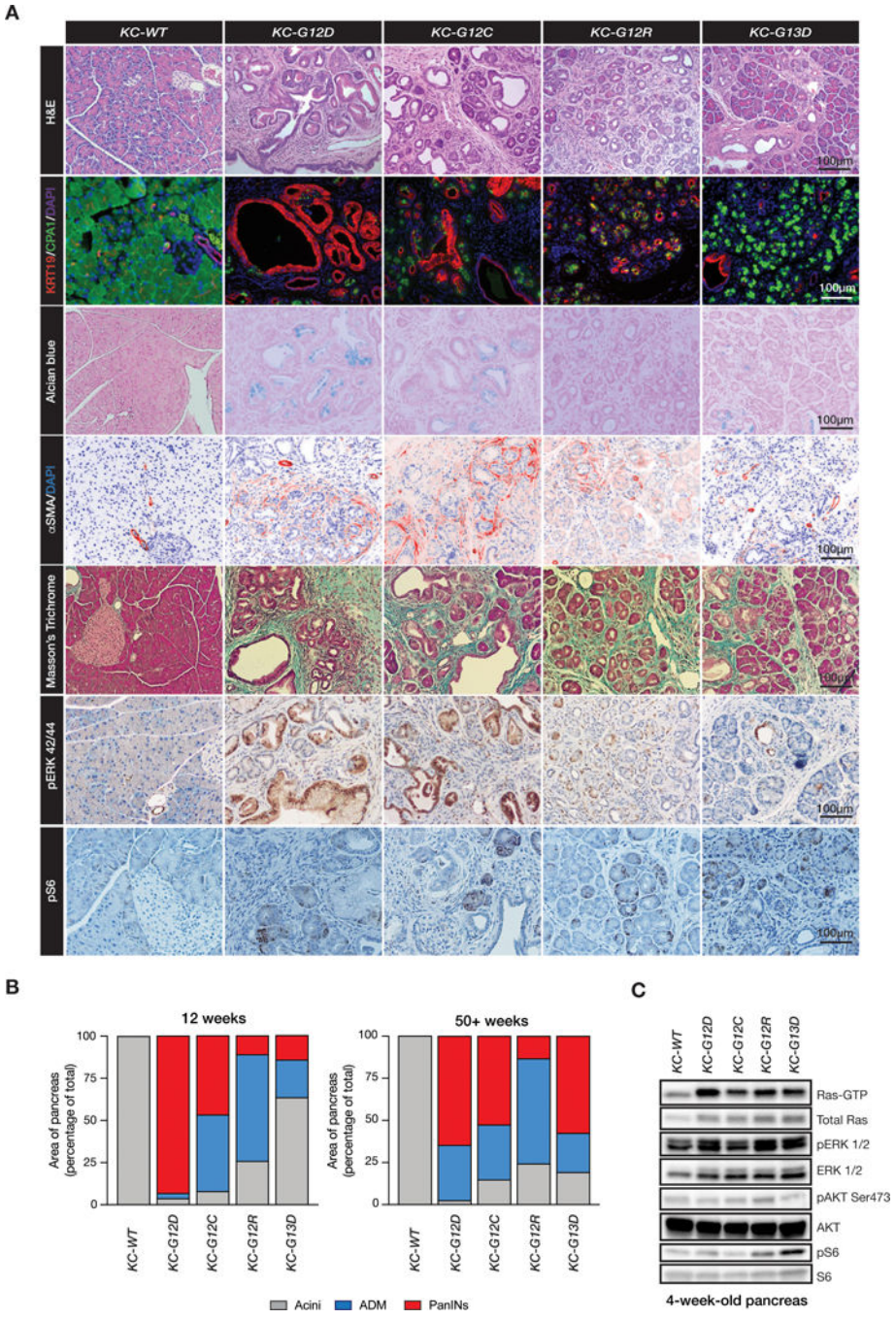

Figure 3. Tumor initiation in pancreas displays a different phenotype in each Kras mutant strain.

A. Histological cross-sections, immunofluorescent and immunohistochemical stains of 12-week-old pancreata from each Kras mutant strain, as indicated. Representative stainings of H&E (right panel) and CPA1/KRT19 displaying acini, acinar-to-ductal-metaplasia (ADM) or pancreatic intraepithelial neoplasias (PanINs) examples. **B.** Graphs show area of pancreatic lesions from 12-week-old and 50-week-old quantified as acini, ADM or PanINs

(n=3–4 mice per genotype). **C.** Ras-GTP levels and activation of downstream signaling from whole pancreas tissue lysates harvested from 4-week-old mice.

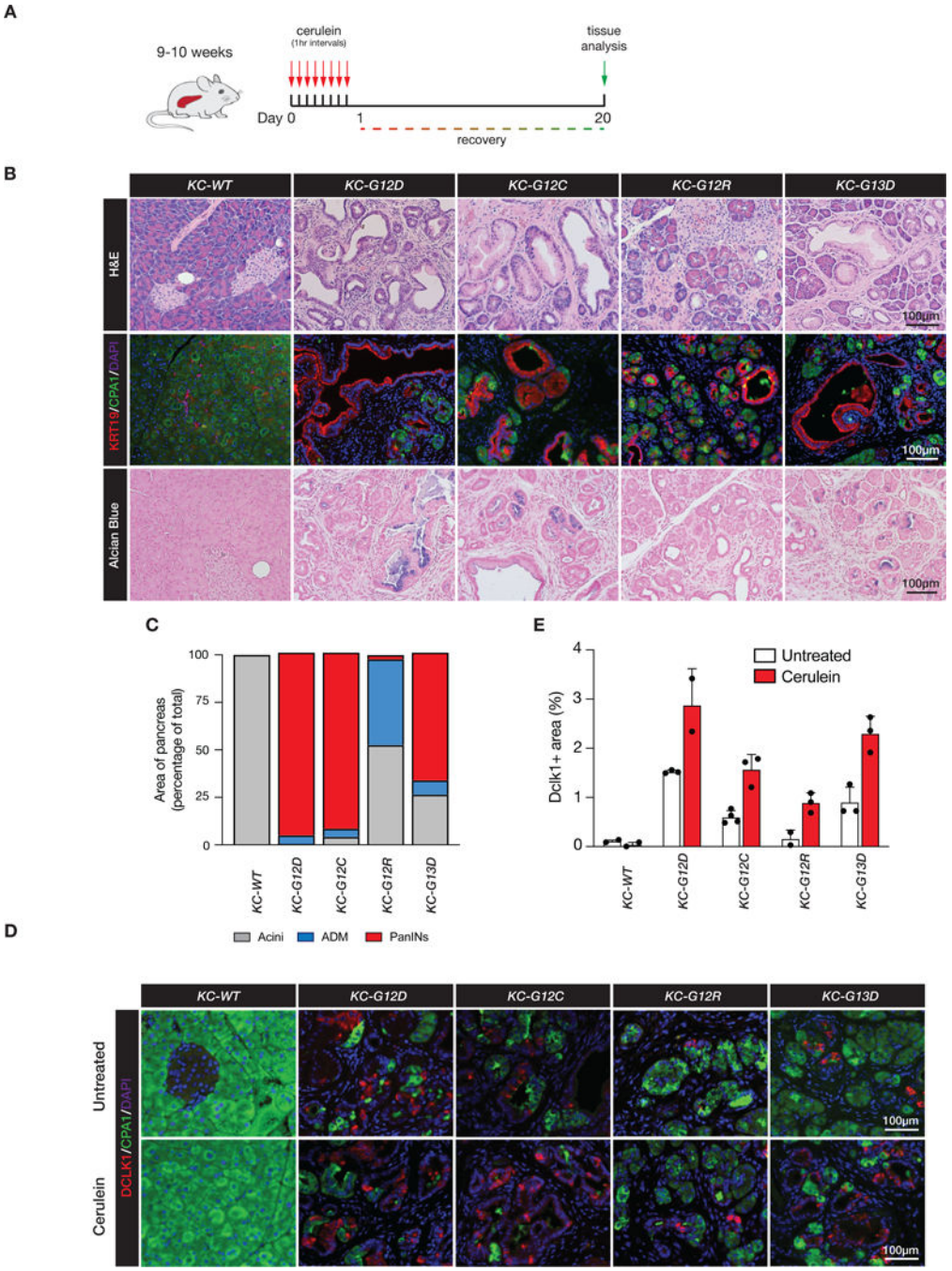

Figure 4. Context-specific disease progression in Kras mutant pancreatic epithelium.

A. Schematic depiction of cerulein acute pancreatitis treatment. **B.** Histological cross-sections, immunofluorescent and immunohistochemical stains of 12-week-old pancreata (20 days following cerulein treatment) from each Kras mutant strain, as indicated. **C.** Area of pancreatic lesions quantified as acini, acinar-to-ductal metaplasia (ADM) or pancreatic intraepithelial neoplasias (PanINs). N=2–3 mice per genotype. **D.** Immunofluorescent staining for DCLK1 in pancreatic tissue sections from untreated or cerulein-treated mice. **E.**

Percentage of DCLK1+ stained area. Error bars are SD, n=2–3 mice per genotype, as indicated.

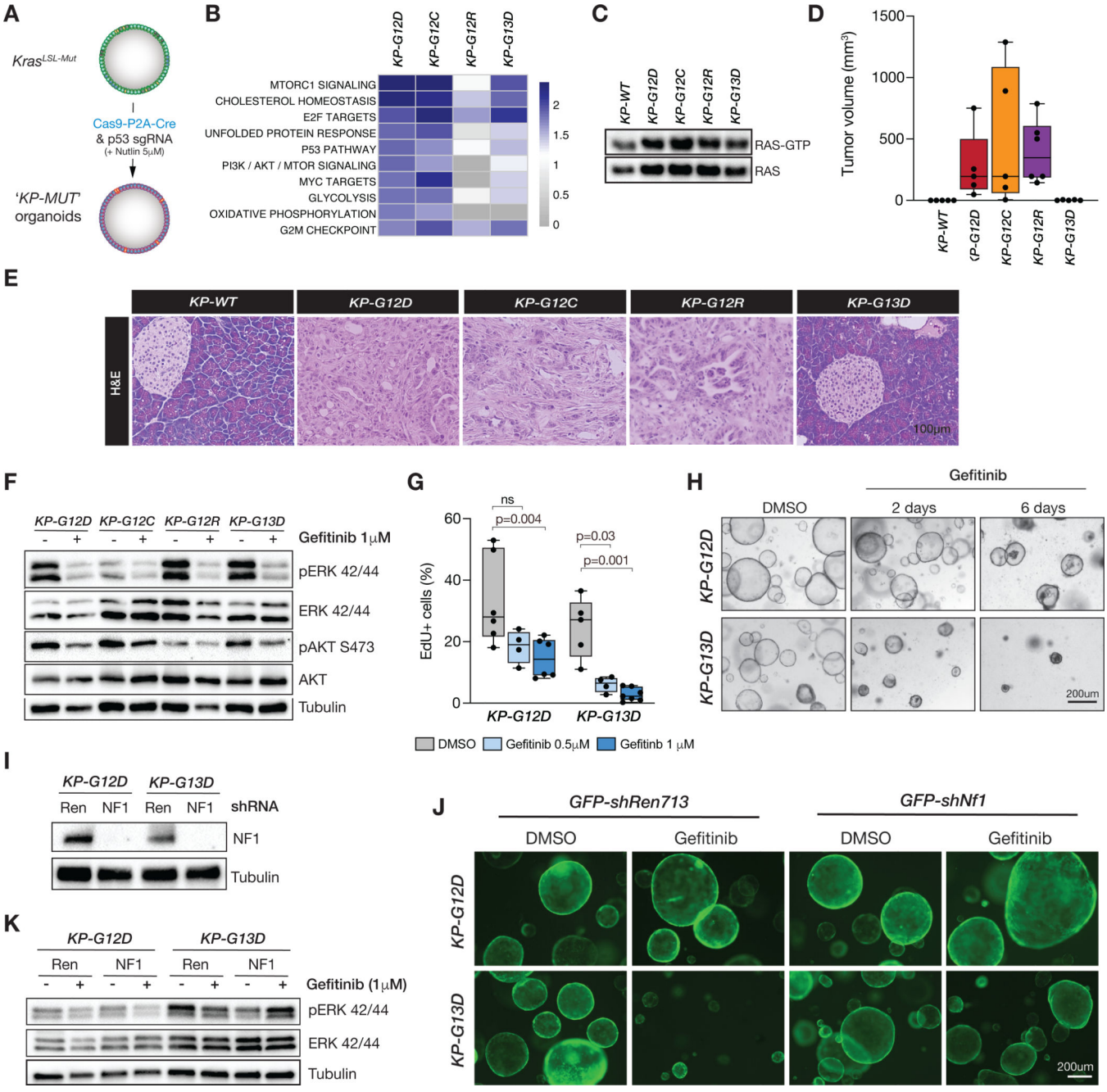

Figure 5. Kras^{G13D} pancreatic organoids are sensitive to EGFR inhibition

A. Kras mutations and p53 loss were created after pancreatic organoids were infected with a vector containing a p53 sgRNA and Cre recombinase, then selected in Nutlin-3 for 10 days. **B.** Gene set enrichment analysis (GSEA) summary displaying the top 10 enriched pathways in KP-G12D organoids, compared to Kras^{WT} organoids ordered by Normalized Enrichment Score (NES). **C**. Ras-GTP levels were determined after culturing them 3 days in *basal media.* **D.** Graph showing tumor volume (measured in mm^3) from harvested pancreata 12 weeks after organoids were orthotopically transplanted. **E.** Histological cross-section from harvested pancreata 12 weeks after organoids were orthotopically transplanted. **F.** Western

blots performed in KP-G12D, KP-G12C, KP-G12R, and KP-G13D organoids following 2 days of Gefitinib or DMSO treatment, showing a decrease in phospho-ERK 42/44 signaling after EGFR inhibition. **G.** EdU flow cytometry from Gefitinib or DMSO-treated KP-G12D and KP-G13D organoids, treated with Gefitinib or DMSO (2 days). Error bars are SD, n=3 independent biological replicates; 2-way ANOVA. **H.** Brightfield images from KP-G12D and KP-G13D organoids treated with DMSO or 1μM Gefitinib for 2 and 6 days. **I.** Western blot showing NF1 knockdown or control shRenilla.713 ("Ren") KP-G12D and KP-G13D organoids. **J.** shNF1 and shRen expressing KP-G12D and KP-G13D organoids treated with DMSO or Gefitinib for 3 days. GFP is linked to expression of the shRNA. **K.** Western blot displaying an increase in ERK 42/44 phosphorylation in Gefitinib-treated KP-G13D organoids after NF1 knockdown.

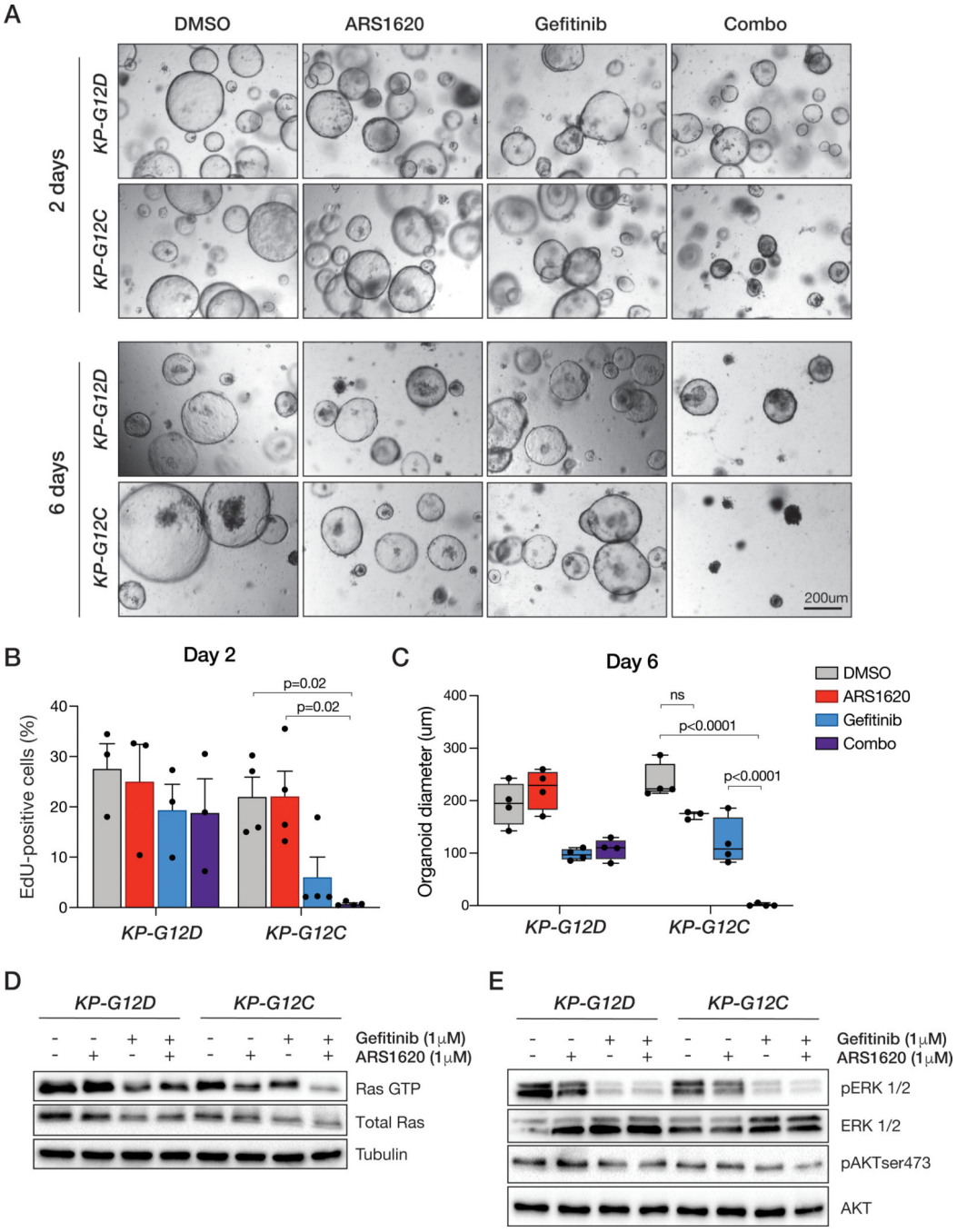

Figure 6. The selective KRAS G12C inhibitor ARS1620 eliminates Kras^{G12C} organoids in combination with EGFR inhibition.

A. Brightfield images showing organoid morphology following 2 (left panel) and 6 days treatments with ARS1620 (1μM), Gefitinib (1μM) or the combination (Combo) treatment in KP-G12D and KP-G12C organoids. **B.** EdU flow cytometry performed at 2 days of treatment. Error bars are SD, n=3–4 independent biological replicates; 2-way ANOVA. **C.** Graph displaying organoid diameter in micrometers (um) at 6 day of treatment; test 2-way ANOVA. Western blot showing Ras-GTP levels (**D**) and ERK/AKT phosphorylation (**E**) in

KP-G12D and KP-G12C organoids 24 hours after treatment either with DMSO, ARS1620, Gefitinib or both inhibitors.